KChIP4a selectively controls mesolimbic dopamine neuron inhibitory integration and learning from negative prediction errors

Kauê M. Costa[1,†,*], Niklas Hammer[1], Christopher Knowlton[2], Jochen Schwenk[3], Tamara Müller[5], Dorothea Schulte[5], Bernd Fakler[3,4], Carmen C. Canavier[2] and Jochen Roeper[1*]

[1] Institute of Neurophysiology, Goethe-University Frankfurt, Theodor-Stern-Kai 7, 60590, Frankfurt am Main, Germany

[2] Department of Cell Biology and Anatomy, Louisiana State University Health Sciences Center, 1901 Perdido Street, 70112, New Orleans, LA, USA

[3] Institute of Physiology, University of Freiburg, Hermann-Herder-Strasse 7, 79104, Freiburg, Germany

[4] Signaling Research Centers BIOSS and CIBSS, Schänzlestrasse 18, Freiburg, 79104, Germany

[5] Edinger Institute, Goethe-University Frankfurt, Theodor-Stern-Kai 7, 60590, Frankfurt am Main, Germany

[†] Current address: National Institute on Drug Abuse Intramural Research Program, National Institutes of Health, Baltimore, USA.

* Correspondence to: roeper@em.uni-frankfurt.de or kaue.m.costa@gmail.com

Abstract

Midbrain dopamine (DA) neurons are essential for multiple behaviors. DA neurons that project to different regions also have unique biophysical properties, and it is thought that this diversity reflects specializations to particular computational functions. If this is true, there should be specific genetic determinants of this heterogeneity whose manipulation would lead to circumscribed impacts on behavior. We test this general hypothesis by homing in on one particular mechanism using a new transgenic model and a combination of molecular, electrophysiological, computational, and behavioral approaches. We demonstrate that KChIP4a, a singular Kv4 β-subunit splice variant, determines the long hyperpolarization-rebound delays observed in nucleus accumbens core-projecting DA neurons, that this biophysical switch controls the efficacy of inhibitory inputs to pause firing and, congruently, selectively regulates learning from negative prediction errors. Our results reveal a highly specialized gene-to-behavior mechanistic chain within the DA system, illuminating how cellular diversity shapes information processing in this key neuronal population.

Keywords: dopamine, mesolimbic, reinforcement learning, A-type current, Kv4, KChIP4, single compartment model, channel-complex proteomics, synaptic integration, reward prediction error

Graphical abstract

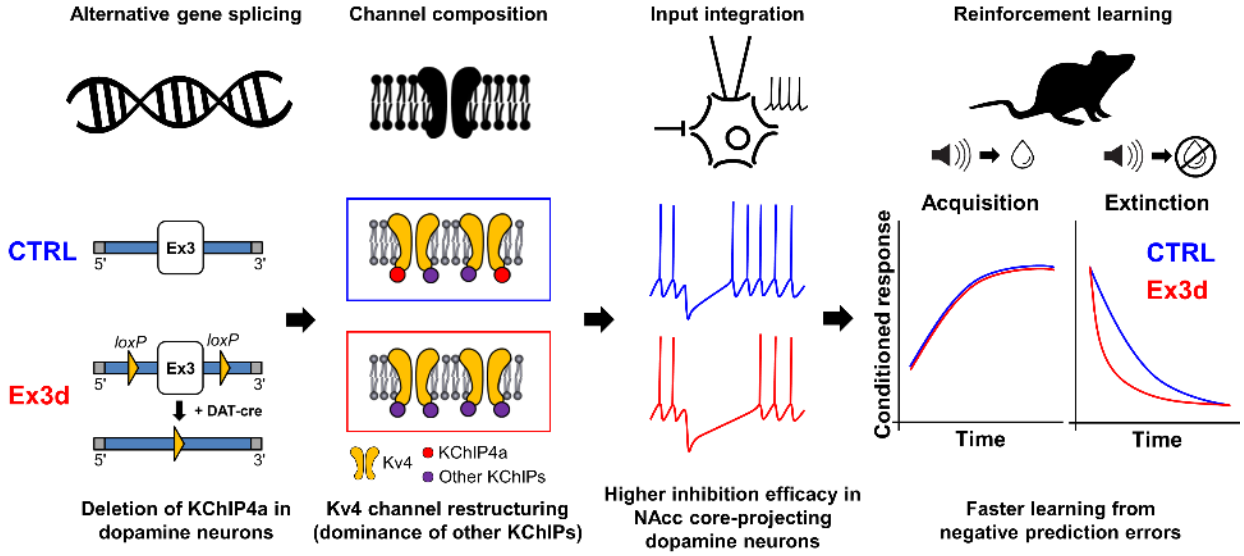

Introduction

Midbrain dopamine (DA) neurons regulate several behavioral functions, particularly learning and motivation, and are implicated in nearly every mental illness (Bromberg-Martin et al., 2010; Schultz et al., 1997). While previously thought to be a homogenous population, work from our lab and others has revealed that these neurons display a wide range of biophysical properties and gene expression profiles, which vary categorically depending on their axonal projection target and define vulnerability to disease (Aguila et al., 2018; Costa, 2014; Farassat et al., 2019; Kramer et al., 2018; Lammel et al., 2008; Lander et al., 2001; Schiemann et al., 2012; Tarfa et al., 2017). But why do projection-defined DA neuron subpopulations have different membrane properties? One hypothesis is that the membrane properties of each subgroup is specialized to a particular behavioral function (Roeper, 2013). If this is the case, it stands to reason that there should also be specific genetic mechanisms within each neuronal group that underpin these adaptations. Another corollary of this hypothesis is that each biophysical variable, by virtue of their contributions to identifiable computational processes, should also have relatively circumscribed influences in behavior. In this study, we test this general hypothesis by homing in on one key biophysical differentiator of DA neuron subpopulations.

Specifically, DA neurons in the ventral tegmental area (VTA) that project to the core of the nucleus accumbens (DA-cNAcc), among select others, display longer rebound delays from hyperpolarizing inhibition than those that project to the lateral shell of the NAcc (DA-lNacc) and the dorsolateral striatum (DA-DLS) (Lammel et al., 2008). Previous studies have demonstrated that atypically slowly inactivating A-type K^+ currents, mediated mainly by Kv4.3 channel complexes, are responsible for these longer delays (Liss et al., 2001; Tarfa et al., 2017). This suggested that Kv4 channels in neurons may be differentially modulated by a so far unknown mechanism.

Kv4 channel function is tightly controlled by the binding of modulatory β-subunits, especially of the KChIP (K^+ channel interacting proteins) family (An et al., 2000; Jerng and Pfaffinger, 2014; Jerng et al., 2004). In mammals, four genes (KCNIP 1-4) encode distinct KChIP proteins, each with multiple splice variants. One of those, KChIP4a (a splice variant of KChIP4) stands out for having a unique K^+ channel inhibitory domain (KID), which, upon binding to the pore-forming subunits, dramatically slows Kv4 channel inactivation (Holmqvist et al., 2002; Jerng and Pfaffinger, 2008, 2014; Tang et al., 2013). In addition, the KChIP4a KID suppresses membrane trafficking of Kv4 channels, due to the presence on an ER-retention motif, and promotes close-state inactivation (Jerng and Pfaffinger, 2008, 2014; Tang et al., 2013). Most other KChIP isoforms, including all other KChIP4 variants, induce the opposite effects, and the ultimate effect on channel kinetics depends on the relative ratio between KChIP4a and other KChIP isoforms within the channel complex (Kitazawa et al., 2014; Tang et al., 2013; Zhou et al., 2015). A differential expression of KChIP4a by DA-cNAcc neurons could potentially lead to longer rebound delays by delaying the inactivation of Kv4 channels, keeping the cells hyperpolarized for longer periods. We therefore reasoned that KChIP4a could be the molecular determinant of the projection-specific diversity in rebound delays across DA neurons.

What would this mean for the role of these cells in behavior? One of the ways in which DA neuron activity is thought to influence behavior is by determining post-synaptic plasticity according to the experience of reward prediction errors (RPEs), i.e. the difference between expected and experienced value (Schultz et al., 1997). It has been extensively demonstrated, across multiple behavioral contingencies, experimental methods and organisms, that some DA neurons respond with phasic increases in firing to unexpected rewards and reward-predicting cues (positive RPEs), and with phasic decreases, or pauses, in firing when an expected reward is omitted or reduced (negative RPEs) (Cohen et al., 2012; Schultz et al., 1997). This is especially true of DA projections to the cNAcc (Hart et al., 2014). While there is controversy on

whether DA neurons symmetrically represent positive and negative RPEs (Bayer et al., 2005, 2007; Dreyer et al., 2010; Hart et al., 2014; Niv et al., 2005), and on how the dynamics of DA neuron firing pauses are related to negative RPE signaling (Bayer et al., 2007; Chang et al., 2017, 2018; Matsumoto et al., 2016), multiple studies have demonstrated that transient inhibition of DA neuron firing is causally implicated in learning from negative RPEs (Chang et al., 2015, 2018; Steinberg et al., 2013; Tian and Uchida, 2015). Building upon this rationale, we predicted that the endogenous expression of the alternative splice variant KChIP4a, by controlling the integration of inhibitory inputs in DA-cNAcc neurons, should play a circumscribed role in regulating learning from negative RPEs.

We tested this set of hypotheses by creating a new cell type- and exon-specific transgenic mouse line where the KChIP4a isoform is deleted only in DA neurons, which allowed us to disrupt this proposed mechanistic chain at its most basic link. Using a combination of molecular, electrophysiological, computational, and behavioral approaches, we show that KChIP4a underlies of one of the key features of DA neuron diversity, and that this regulates inhibition integration and learning from disappointment.

Results

Selective deletion of KChIP4a from midbrain DA neurons

To selectively knock out KChIP4a in DA neurons, we developed a mouse line where we floxed the exon coding for the KID of KCNIP4 (exon 3), which is unique to the KChIP4a variant (Figure 1A and B) (Holmqvist et al., 2002; Jerng et al., 2004). We then crossed these mice with a DAT-Cre line to create mice with a selective deletion of KChip4a in midbrain DA neurons (Ex3d, for “exon 3 deletion”, Figure 1C). For all subsequent procedures, these mice were compared with their heterozygous DAT-Cre knock-in littermate controls (CTRL) (Costa et al., 2021).

To validate the effects of our conditional exon-specific knockout, we used a combination of fluorescence in situ hybridization (FISH) with probes for both the KID n-terminal sequence (specific to the KChIP4a isoform) and for the conserved KChIP4 c-terminus (to label all KChIP4 variants), combined with immunohistochemistry (IHC) for tyrosine hydroxylase (TH) to identify DA neurons. We observed clear double-labeling for both KChIp4a mRNA and TH in the midbrain of CTRL mice, but no such labeling was seen in Ex3d mice (Figure 1D). Labeling of KChIP4a mRNA was visible in TH- cells in both CTRL and Ex3d mice, confirming that our mutation ablated KChIP4a mRNA expression only in TH+ DA neurons (Figure S1J). Finally, when using the probe that labels all KChIP4 variants, we observed labeling in TH+ cells in both CTRL and Ex3d mice (Figures S1E and K), demonstrating that the Ex3d mutation did not eliminate expression of other KChIP4 variants in midbrain DA neurons.

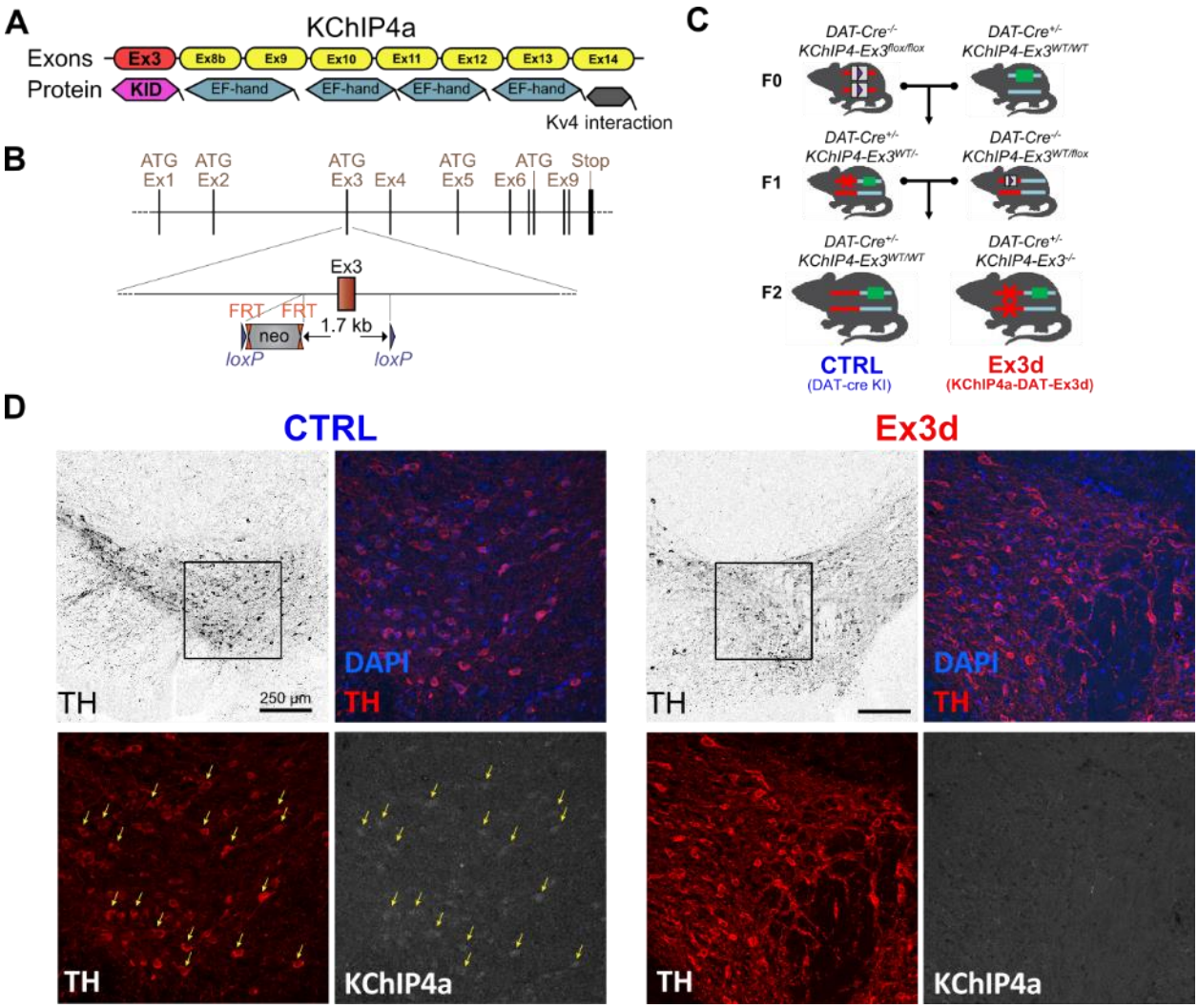

Figure 1. A new transgenic mouse line where KChIP4a is selectively deleted from DA neurons.

A: Cartoon schematic of KChIP4a exons and corresponding proteins. Note that the KChIP4a-defining KID is encoded by Ex3 of the KCNIP4 gene. **B:** Cartoon schematic of the transgenic strategy used for creating the vector where Ex3 was floxed. This vector was later electroporated into mouse embryonic stem cells which were subsequently used to generate mice with a Cre-dependent conditional KO of KCNIP4 Ex3 (see Methods section for details). **C:** Breeding strategy for generating mice with a selective deletion of KChip4a in midbrain DA neurons (Ex3d). Conditional KO mice were crossed with DAT-Cre KI mice (F0), generating double heterozygous offspring (F1), which were then crossed to produce Ex3d mice and controls that were DAT-Cre KI but did not have floxed KCNIP Ex3 (CTRL). **D:** FISH validation of the KO strategy, including overviews of the midbrain TH and DAPI stain and TH and KChIP4a co-labeling, or lack thereof. CTRL mice showed robust expression of KChIP4a mRNA in midbrain DA neurons, while Ex3d mice showed no such expression (see Figure S1 for additional validation).

Ex3d mutation changes midbrain Kv4 channel composition

To evaluate the effects of the Ex3d mutation on ion channel composition, we used quantitative high-resolution mass spectrometric analysis of Kv4 channel complexes (Figures 2 and S2) affinity-purified from tissue samples of midbrain (region of interest) or cerebellum (control region) from both CTRL and Ex3d mice (Bildl et al., 2012; Muller et al., 2016; Schwenk et al., 2012). We found that, in both regions, the average Kv4.3 tetramer was composed of 1 Kv4.2 and 3 Kv4.3 pore-forming units, likely a result of Kv4.3 homo- and hetero-tetrameric configurations. Within the midbrain, the average Kv4 channel is bound to 1 KChIP1 or KChIP2, 1 KChIP3, and 2 KChIP4, indicating that KChIP4 is the dominant regulatory subunit in this region (Figure 2A). In the cerebellum, the KChIP stoichiometry is slightly altered, averaging 1 KChIP1 and 1 or 2 KChIPs 3 and 4, with only a minor contribution of KChIP2, which highlights that the dominance of KChIP4 in the midbrain is region-specific (Figure 2B). Importantly, there was no significant difference in the relative abundance of any Kv4 channel complex protein between CTRL and Ex3d mice, in both the midbrain and cerebellum. This confirms that the Ex3d mutation not only does not disrupt expression of other KChIP4 variants, but also spares the binding stoichiometry of the general KChIP families.

In addition, we quantified the relative abundance of KChIP4a in each tissue sample and found a selective reduction of the respective protein amounts in the midbrain samples from Ex3d mice (Figure 2C). This reduction is not complete (~20%), likely because non-dopaminergic cells within the midbrain still express KChIP4a in Ex3d mice (Figure S1J), which is concordant with a targeted disruption of KChIP4a expression in midbrain DA neurons.

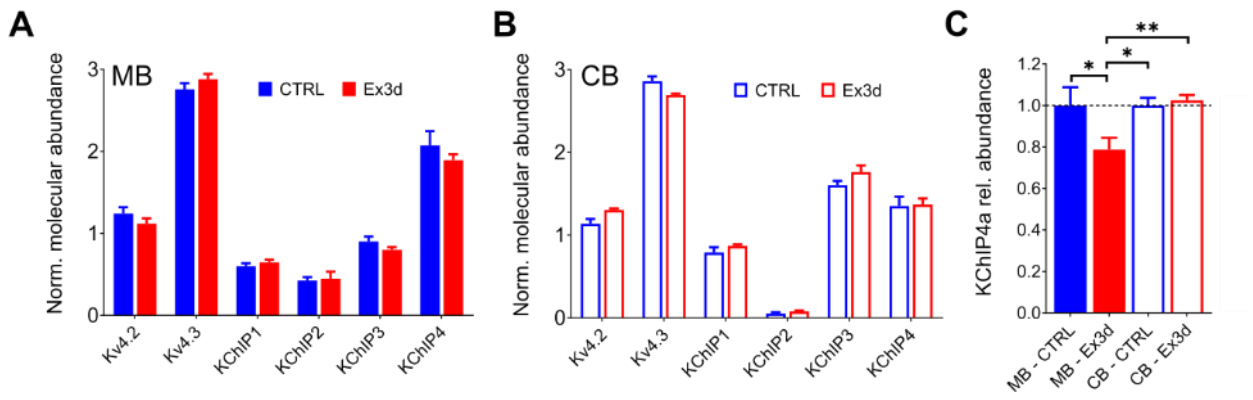

Figure 2. Ex3d mutation reduces KChIP4a expression in midbrain DA neurons without disrupting overall Kv4 channel subunit composition.

A: Normalized molecular abundance of Kv4 complex subunits within the ventral midbrain (MB) of both CTRL and Ex3d mice (see also Figure S2). Data is normalized to the tetrameric structure of the channel complex. Kv4.3 is the predominant pore-forming subunit, and KChIP4 isoforms are the predominant KChIP regulatory partners (averaging 2/4 in each tetramer). There was no significant difference in the general stoichiometry of different Kv4 or KChIP variants between CTRL and Ex3d mice. **B:** Analysis, as in A, performed in cerebellum (CB) of the same mice. Note that Kv4.3 is the most abundant pore-forming subunit, but the stoichiometry of the KChIP subunits differed from that of the midbrain. **C:** Detailed analysis of KChIP4a protein abundance (relative to CTRL). Note the selective reduction in the abundance of this protein in the MB of Ex3d mice, in line with predicted effects of the Ex3d mutation and the FISH results (Figure 1). Error bars indicate standard error of the mean. *P < 0.05; **P < 0.01.

KChIP4a regulates rebound delays and inhibition integration in mesolimbic core DA neurons

To test whether KChIP4a was the molecular determinant of the relatively long rebound delays observed in cNAcc-DA neurons (Lammel et al., 2008; Tarfa et al., 2017), we performed *in vitro* patch-clamp recordings of DA neurons from Ex3d and CTRL mice that projected to the NAcc core, NAcc lateral shell, or DLS, which were identified by retrograde axonal tracing using red retrobeads and had their neurochemical identity confirmed with post-hoc TH IHC (Figure 3A, B and C) (Lammel et al., 2008). We found that the Ex3d mutation selectively reduced the rebound delay in cNAcc-DA neurons by nearly 50% (Figure 3D and H). There was no effect of the KChIP4a deletion on nearly all of the membrane properties of DA neurons that projected to the

other striatal areas (Figure 3I and J), nor was there any effect additional effect in DA-cNAcc neurons (Figure 3H), including no change in firing rate, sag potential, action potential threshold and other variables (Figure S4). The only exception was a small but significant increase in the minimum afterhyperpolarization voltage in DA-DLS neurons (Figure S4C). These results confirm our hypothesis that KChIP4a is the main determinant of the long rebound delays observed in the DA-cNAcc neuron subpopulation. Furthermore, this effect is highly biophysically selective, as almost no other variable was affected by the Ex3d mutation.

Simulation of KChIP4a deletion effects predicts a counter-intuitive increase in inhibition efficacy

Given the multiple effects of KChIP4a on Kv4 channel properties (Holmqvist et al., 2002; Jerng and Pfaffinger, 2008, 2014; Tang et al., 2013), the ultimate consequence of its removal on behaviorally-relevant neural activity could depend on several factors. In order to form a specific hypothesis for the behavioral consequences of KChIP4a deletion in DA neurons, we needed to infer how this manipulation would affect input processing across different conditions of synaptic connectivity and temporal integration. As it would be unfeasible to tackle the parameter space for such a comparison experimentally, we used biophysically realistic computational models of DA-cNAcc neurons (Figure 4), tailored to reflect their empirically defined membrane properties (Knowlton et al., 2021).

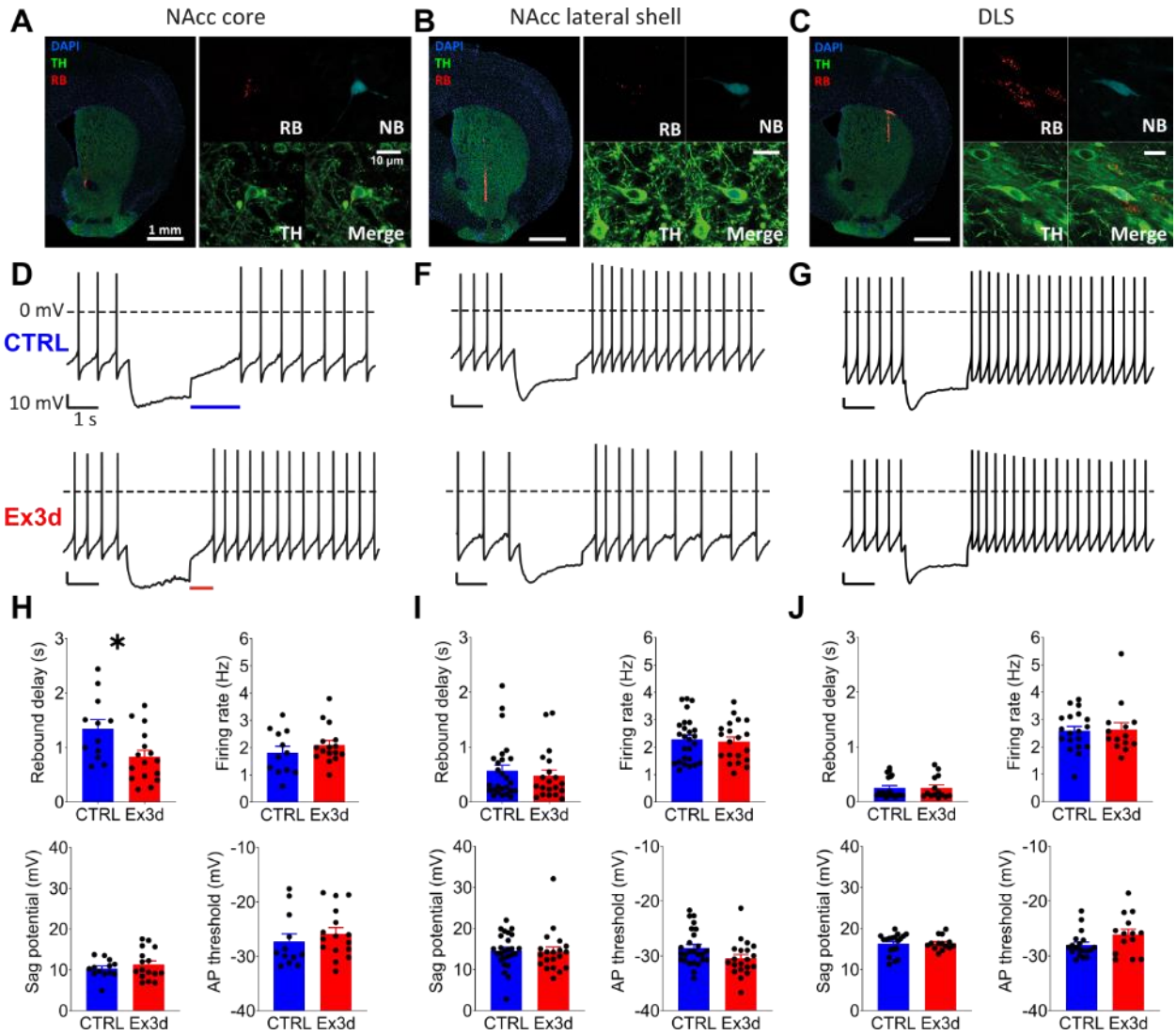

Figure 3. KChIP4a is responsible for the longer rebound delay seen in NAcc core-projecting DA neurons.

A, B, C: Representative micrographs of red retrobeads (RB) injections in the NAcc core (A), lateral shell (B) and DLS (C), as well as of recorded, retrogradely-labeled, and TH-stained DA neurons from each of the projection pathways (See Figure S3 for the full mapping of injection and recording sites). **D, F, G**: Representative current-clamp recordings of DA neurons from both CTRL and Ex3d mice with confirmed projections to the NAcc core (D), lateral shell (F) or DLS (G), in response to current injection hyperpolarizing the membrane potential to -80 mV. Note the shorter rebound delay in the NAcc core-projecting example from an Ex3d mouse in relation to CTRL. **H, I, J:** Biophysical properties of projection-identified DA neurons from CTRL and Ex3d mice. See Figure S4 for more comparisons. AP = action potential. Error bars indicate SEM. *P < 0.05.

First, to simulate the effects of binding of different KChIPs, we fitted the activation and inactivation kinetics of Kv4.3 channels to reflect binding of “fast” KChIPs (KChIP1-3 and other KChIP4 variants), which amplify peak current amplitudes and accelerate inactivation, or KChIP4a, which has the opposite effects (Figure 4A) (Holmqvist et al., 2002). We then systematically examined the effects of varying the ratio of KChIP4a to fast KChIP binding, and found that a value of 5:4 was found to best approximate the A-type current kinetics of wildtype DA-cNAcc neurons (Tarfa et al., 2017). We used these parameters to simulate neurons from CTRL mice, while to simulate neurons from Ex3d mice we used a completely fast KChIP-bound Kv4.3 current to recapitulate the KChIP4a deletion (Figure 4 B1). Importantly, we found that this was sufficient to fully reproduce the experimentally observed decrease in rebound delay in Ex3d DA-cNAcc neurons (Figure 4B2).

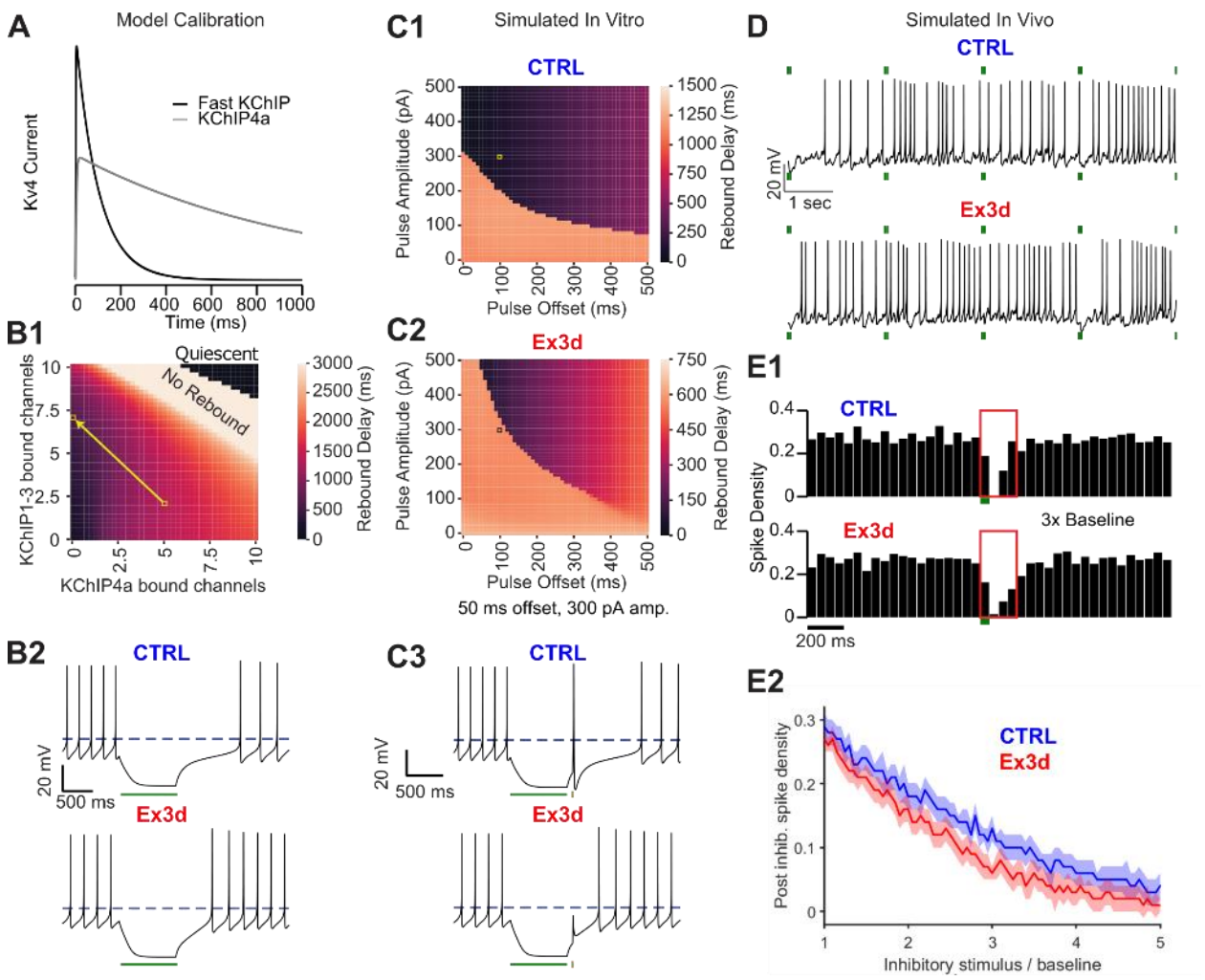

Figure 4. Modelling of the biophysical effects of KChIP4a deletion in DA neurons predicts enhanced *in vivo* firing pauses after inhibition in Ex3d mice.

A: Simulated difference current in response to voltage clamp steps from -100 mV to 0 mV for a model of all Kv4.3 bound to fast KChIPs (black) compared to one in which all Kv4.3 is modeled as bound to KChIP4a (grey). Note lower peak current and slower inactivation with KChIP4a bound model. **B:** Decreasing KChIP4a bound Kv4.3 into fast domain analogs generally decreases rebound delay. **B1:** Heatmap of rebound delay vs fast, slow Kv4.3 conductance. Yellow arrow denotes transition of representative example of control cell (center) to Ex3d cell (top left). Each unit of KChIP1-3 bound KChIP1-3 was assigned a conductance of 120 μS/cm^2 whereas each unit of KChIP4a bound Kv4 was assigned a conductance of 60 μS/cm^2. Excessive total Kv4.3 conductance creates a non-physiological state with no rebound spiking (black region in upper right). **B2:** Voltage trace of representative CTRL and Ex3d cell to a one second current pulse that hyperpolarizes the model to -80 mV (green bars). **C:** Ex3d model is less likely to spike in response to a brief depolarization during the rebound delay. **C1 and C2:** Heat map of rebound delay vs post rebound initiation time (pulse offset) and pulse amplitude for a 10 ms pulse applied during rebound ramp for control (C1) and Ex3d (C2) models. **C3**. The same simulation as in panel B2, with an additional 300 pA current applied 100 ms after offset of the one second hyperpolarizing current pulse for representative CTRL cell (yellow square in C1) and Ex3d cell (black square in C2). **D.** Voltage trace of 3+ trial cycles (2 s intervals) of representative CTRL and Ex3d cells under a simulated *in vivo* environment of balanced NMDA excitation and $GABA_A$ inhibition. Inhibition is intensified by a factor of three (300 Hz mean IPSP rate vs 100 Hz baseline) during 50 ms pulses (blue bars). **E.** Spike density histogram of 500 trials (1000 s) of balanced state *in vivo* firing with 50 ms intervals of elevated inhibition (blue bar at center) for representative CTRL and Ex3d neurons. Red rectangle denotes region of expected pause over which the spike densities in panel F were computed. Note that the repeated single neuron trials can be used to estimate population response to phasic inhibitory signals in the simulated excitation/inhibition balanced *in vivo* state. **F.** Average spike density of bins in pause interval (red square in E) of representative CTRL (blue) and representative Ex3d (red) as a function of the ratio of the rate of IPSP events in the inhibitory signal relative to the baseline rate of IPSPs (100 Hz) generated by a Poisson process. Error bars are the standard deviation of the 1 s pre-pulse interval.

Next, we explored how these different Kv4.3 currents affect the integration of excitatory inputs during rebound delays (when these currents exert their maximum influence on membrane voltage). We did this by applying 10 ms pulses of depolarizing current of variable magnitudes and intervals following the termination of a hyperpolarizing pulse that brought the cell to -80 mV

(Figure 4C). Surprisingly we found that, while KChIP4a deletion reduced the maximum duration of post-hyperpolarization pauses in the absence of excitatory inputs (the condition in which rebound delays, and indeed most biophysical properties, are typically tested), it also reduced the likelihood of an excitatory input to trigger spiking during the same period due to shunting. This was true across a wide range of stimulus amplitudes and offsets (Figure 4C2). This means that, in the presence of excitatory inputs, the deletion of KChIP4a can, counterintuitively, lead to more effective hyperpolarization-induced pausing.

To probe the potential consequences of this finding to the processing of behaviorally relevant information, we tested how CTRL and Ex3d cells would respond in a condition that mimicked as closely as possible the synaptic environment in an intact mouse (a "simulated *in vivo*" model; Figure 4D and E). We did this by applying simultaneous Poisson process trains of excitatory and inhibitory postsynaptic potentials (EPSPs and IPSPs, respectively), to create a balanced state similar to what has been experimentally observed in DA neurons *in vivo* (Otomo et al., 2020). We then applied phasic inhibitory pulses by transiently increasing $GABA_A$ IPSP frequency over multiple trial cycles (Figure 4D). This is similar to what is thought to underlie negative RPE signaling (Cohen et al., 2012). We found that similar increases in IPSP frequencies were significantly more effective in reducing spiking probability in Ex3d cells when compared to CTRLs (Figure E1). This was robust across a wide range of inhibition magnitudes (Figure E2), suggesting that KChIP4a deletion generally enhances the effectivity of pausing *in vivo*. Taken together, our *in silico* exploration of the effects of KChIP4a deletion in DA-cNAcc neurons predicts that Ex3d mice would show more effective hyperpolarization-induced pausing *in vivo*, which should consequently enhance learning from negative RPEs.

KChIP4a deletion in DA neurons selectively enhances learning from negative RPEs

We subjected Ex3d mice and CTRL to a battery of DA-sensitive tasks to test how the deletion of KChIP4a in DA neurons would affect behavior. This included open field exploration (Figure 5A), hole board exploration (Fig 5B), novel object preference (Figure 5C), and spontaneous alternation in the plus maze (Figure 5D). There was no difference between the genotypes in any of these tasks, indicating that deleting KChIP4a in DA neurons did not impact locomotion, anxiety, spontaneous exploratory behavior, novelty preference and learning, short-term memory, nor working memory. This series of tests demonstrated that KChIP4a deletion in DA neurons does not produce a widespread effect on DA-dependent tasks.

To test the model-inspired hypothesis that learning from negative RPEs should be increased by KChIP4a deletion, we trained mice on a reinforcement learning task where they learned that an auditory cue signaled the availability of sugar water reward (acquisition), followed by sessions where reward was omitted (extinction) (Steinberg et al., 2013). We did not observe a significant difference between genotypes on any behavioral variable during acquisition (Fig 6A-D). However, we found that, as predicted by our biophysical modelling, Ex3d and CTRL mice differed dramatically in extinction learning. The Ex3d group displayed a significantly accelerated reduction in the time they spent in the reward port during cue presentation (interaction effect, $F_{5, 135} = 3.2$, $P < 0.01$; Fig 6A) and a faster increase of response latency (interaction effect, $F_{5, 135} = 2.615$, $P < 0.05$; Fig 6B) across extinction sessions.

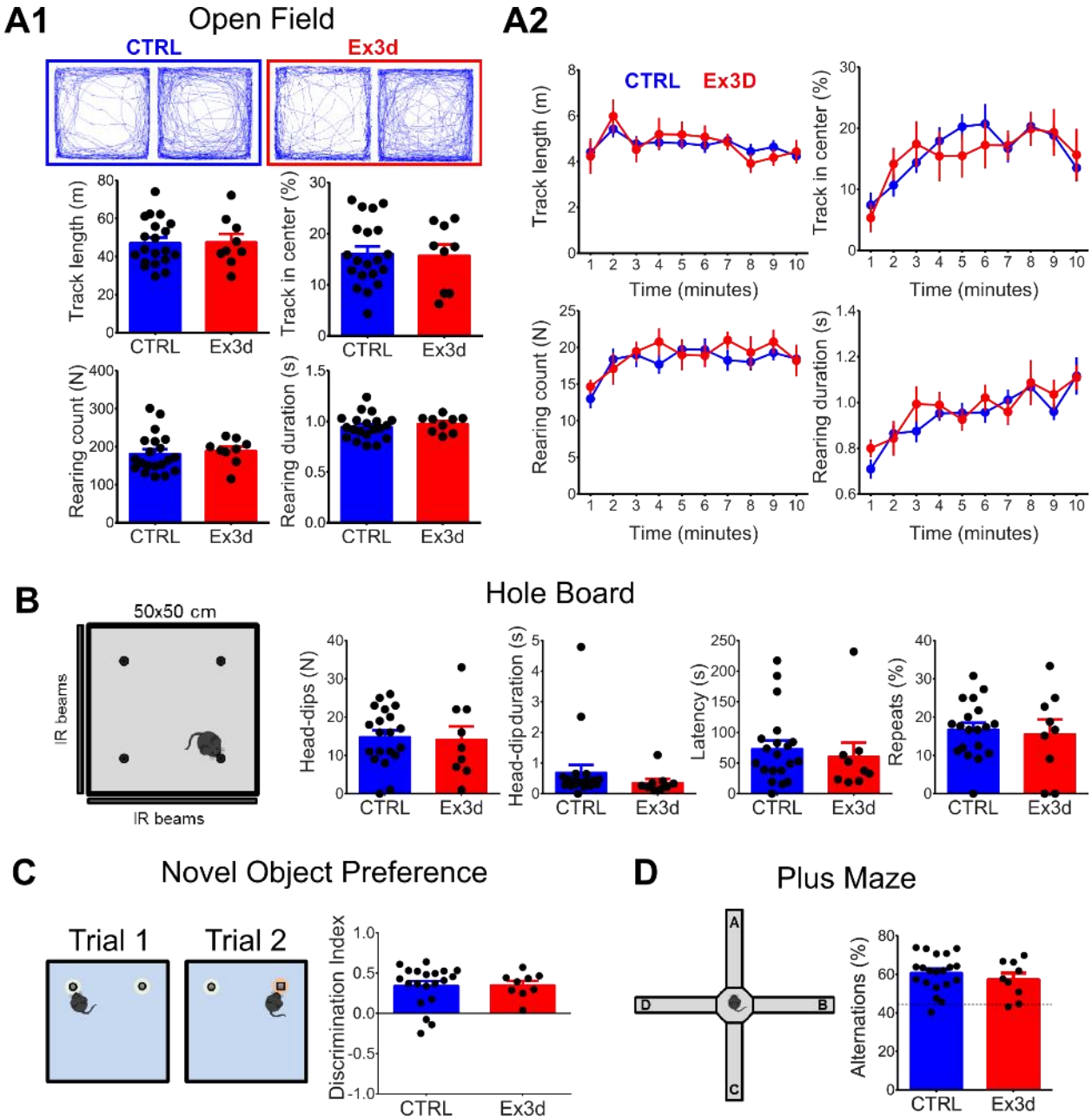

Fig 5. KChIP4a deletion from DA neurons does not affect several DA-dependent behaviors.

A1: Session-based results of the open field test, including representative tracks from mice of both genotypes, averages of the total track length, proportion of track length in the center of the open field, and number and duration of rearings during the 10 minutes of the task. **A2:** same variables as in A1 but averaged across every minute of the 10 minute task. **B:** Hole board test results, including total number of head dips, total summed head-dip durations, latency to first dip and of repeat head-dips. **C:** Cartoon representation of the novel object preference test, and the results of the discrimination index (positive values indicate preference for the novel object in trial 2). **D:** Plus maze test results; spontaneous alternations were evaluated by tracking the order of entry into each arm and quantified as the proportion

of spontaneous alternations in relation to the total possible alternations. Note the absence of a significant genotype difference for all variables in all tests (unpaired T tests and two-way repeated measures ANOVA, P > 0.05). Male and female mice were used, > 8 weeks old, N = 9 for Ex3d and N=20 for CTRL. Error bars indicate SEM.

To verify whether we were observing a direct effect on learning (which would be compatible with an impact on RPE signaling) or a reduction of responding in the absence of direct reinforcement (more compatible with an impact on motivational processes), we analyzed the trial-by-trial behavior measures in the first extinction session. If the Ex3d mice already displayed a reduced time in port on the first extinction trial (when the mice were first confronted with an unexpected reward omission), then the genotype effect would be more likely attributable to decreased motivation (Berridge, 2012). However, we found that Ex3d and CTRL mice were statistically indistinguishable in their responses during the first extinction trial (Fig 6A-D). Only in later trials of the first extinction session, genotype differences emerged in response latency (interaction effect, $_{F9,\ 243}$ = 2.01, P < 0.05; genotype effect, Ex3d > DAT-Cre KI, $F_{1,\ 27}$ = 7.51, P < 0.05; Fig 6B) and in the number of head entries (genotype effect, CTRL > Ex3d, $F_{1,\ 27}$ = 5.98, P < 0.05; Fig 6C). We also identified a strong trend for a gradual divergence between genotypes, starting on the second trial, for the time in port metric (genotype effect, CTRL > Ex3d, $F_{1,\ 27}$ = 3.51, P = 0.07; Fig 6A). This confirms that the Ex3d effect progressively developed as the mice learned that the CS no longer predicted US availability, strongly suggesting a selective effect on learning from expected reward omission, i.e. negative RPEs.

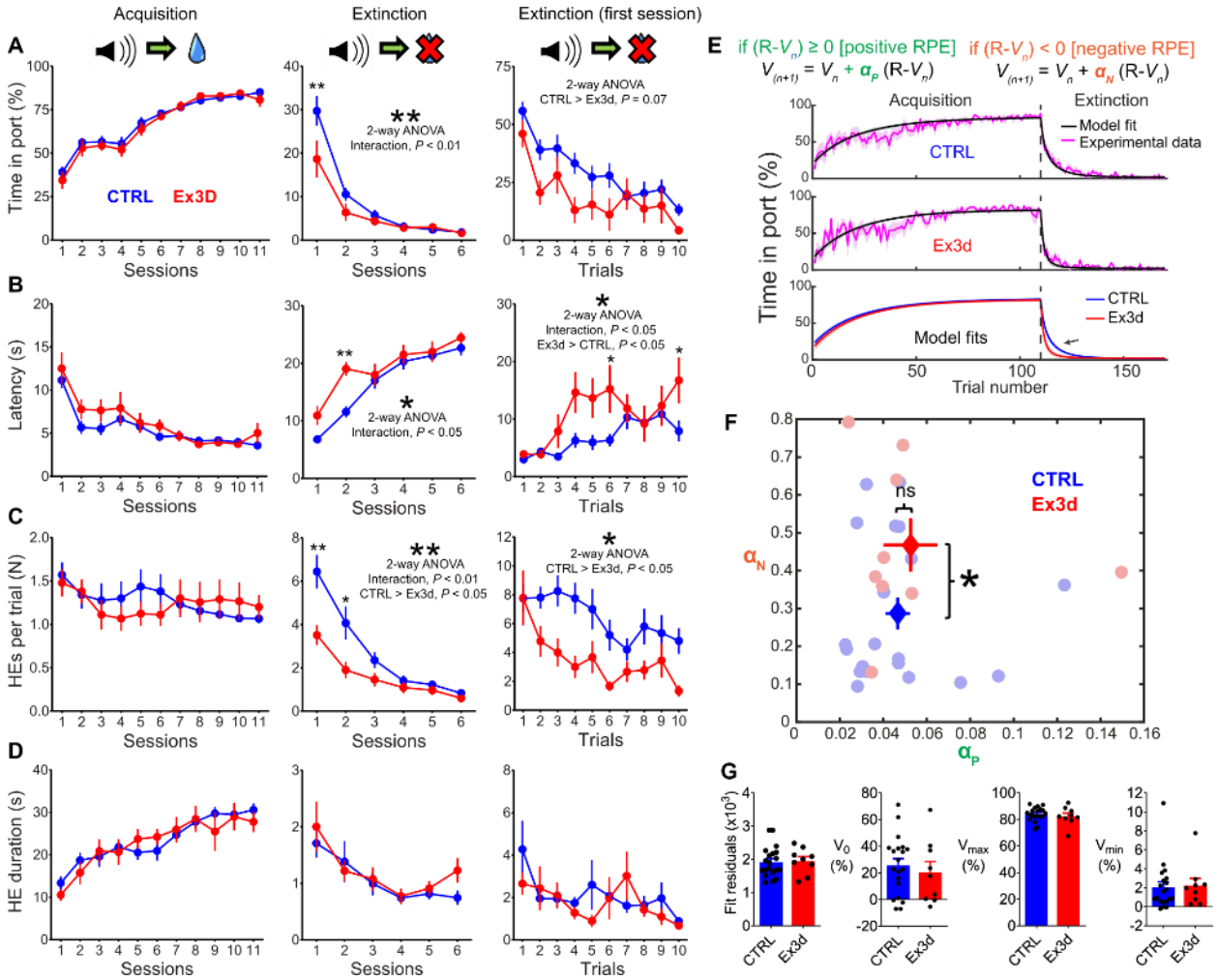

Fig 6. DA neuron-specific KChIP4a deletion selectively improves learning from negative RPEs. **A:** Time spent in port during CS presentation on a session-by-session basis during acquisition and extinction, as well as on a trial-by-trial and session average basis on the first extinction session. Note the faster response extinction for Ex3d mice in relation to controls, including the significant pair-wise difference during the first extinction session, and the strong trend towards faster trial-by-trial extinction in the first extinction session. **B:** Latency to respond during CS presentation for all phases of the reinforcement learning task. This measure increased faster during extinction in Ex3d mice. Importantly, there was also faster trial-by-trial learning in the first extinction session. **C:** Number of head entries into the reward port during CS presentation. Note the faster response extinction for Ex3d mice in relation to CTRL, as well as a faster trial-by-trial extinction in the first session of extinction in Ex3d mice. **D:** Duration of head entries into the reward port during CS presentation. Note the lack of a genotype effect during all phases of acquisition and extinction. Furthermore, for all measured variables, there was no significant difference between genotypes during acquisition or in the first trial of the first session of extinction. **E:** Fitting of a modified Rescorla-Wagner model to the trial-by-trial time in port experimental data of the CTRL and Ex3d groups. Note that the model tracks the behavioral data with relatively good accuracy in

both groups, and that the model fits overlap almost completely during acquisition, but diverge in extinction, reflecting the faster extinction learning kinetics of the Ex3d mice in relation to controls (black arrow). **F:** Combination of best fit α_P and α_N values for Ex3d (red) and CTRL (blue) groups. Faded circles represent individual values. Large solid crosses indicate the mean ± SEM of each group. Note the selective increase in α_N (learning from negative RPEs) in Ex3d in relation to littermate controls. **G:** V_0, V_{min}, V_{max}, and best fit residuals for Ex3d and CTRL groups. No significant difference was observed between the compared groups. Male and female mice were used, > 8 weeks old, N = 9 for Ex3d and N=20 for CTRL. Error bars indicate SEM. *P < 0.05; **P < 0.01.

To formally test the hypothesis that only negative RPEs were affected, we fitted the trial-by-trial time in port values for both Ex3d and CTRL groups with a modified Rescorla-Wagner model which assumed different learning rates for positive (α_P) and negative (α_N) RPE-based learning, and that the time in port was a linear readout of the associative strength (V) (Raczka et al., 2011; Rescorla and Wagner, 1972; Tian and Uchida, 2015). This model successfully fit the behavioral data, including the different learning kinetics during extinction (Fig 6E). Comparisons of the learning rates for the best fits (lowest absolute residual) showed that indeed the Ex3d group had significantly higher α_N values, i.e. faster learning from negative RPEs ($P < 0.05$), without any change in α_P (Fig 6F). Importantly, empirically derived model constraint parameters (V_0, V_{max} and V_{min}), as well as the goodness of fit (measured by the residuals between the experimental data and the model output), were similar for both genotypes (Fig 6G). These results support the interpretation that the effect of deleting KChIP4a in DA neurons can be explained by a selective increase in learning from negative RPEs.

Discussion

In this study, we disrupted a specific genetic mechanism – the alternative splicing of the Kv4 channel regulatory subunit KChIP4a – in DA neurons and tracked the selective effects of this perturbation on ion channel composition, membrane properties, information integration, and

behavior. We achieved this by generating a transgenic mouse line where only KChIP4a is selectively removed from DA neurons, confirming the selectivity of our molecular perturbation at the level of mRNA and Kv4 channel complex composition using FISH and high-resolution proteomics.

We then showed that DA neuron-specific KChIP4a deletion significantly and selectively reduced rebound delays in DA-cNAcc neurons, sparing both other physiological variables within these neurons and nearly all properties of DA-lNAcc and DA-DLS neurons. This was a crucial step, as it demonstrated that KChIP4a is the molecular determinant of the previously described variability in rebound delays between different subpopulation of DA neurons (Lammel et al., 2008; Tarfa et al., 2017). The subpopulation specificity of this phenotype is likely due to the intrinsic differences in the expression KChIP4a between the cell groups – DA-cNAcc neurons may just express more KChIP4a and are thus more sensitive to its deletion. It could also be determined by differences in HCN currents, which typically oppose the effects of A-type currents by accelerating rebound delays. Cells that barely have sag currents, like DA-cNAcc neurons, would have a limited range for compensating the effects of KChIP4a deletion, while cells with more sag could potentially adjust HCN channel expression to match the changes in Kv4 channel properties. It is also possible, or even probable, that both mechanisms are involved in determining the final phenotype. The biophysical selectivity of the phenotype could be attributable to the fact that Kv4 channels are mostly inactivated at typical neuronal resting potentials and require hyperpolarization to recover from inactivation (Jerng et al., 2004), i.e. they contribute little to the cell's electrophysiological dynamics unless there is hyperpolarizing inhibition.

With these findings in hand, we used biophysical computational models of DA-cNAcc neurons to simulate the effects of KChIP4a deletion across a wide variety of conditions. Crucially, we used Poisson-distributed IPSP and EPSP trains to simulate how this genetic manipulation should affect information integration *in vivo*, an approach we found most useful. We demonstrate that

removal of KChIP4a is sufficient to shorten rebound delays like we observed in our in vitro experiments (which strengthens our previous finding), but it also leads to an apparently paradoxical increase in pausing efficiency when considering concurrent excitatory inputs. While at a first glance this seems counterintuitive, it is easily understood when one takes into account the dual effect of KChIP4a in suppressing both Kv4 inactivation and membrane expression (Holmqvist et al., 2002; Tang et al., 2013). Basically, the faster inactivation reduces maximum pause duration, but the increase in peak current due to unrepressed membrane trafficking more effectively shunts excitation. Our simulations thus predicted, correctly, that negative RPE signaling would be enhanced in Ex3d mice. Importantly, our simulated *in vivo* approach allowed us to conceptually overcome some of the confounds associated with predicting behavioral consequences from *in vitro* physiology, including the fact that most slice experiments do not account for the excitation-inhibition balance that occurs *in vivo*.

Finally, we show that the Ex3d mutation leads to a highly specific change in extinction learning, with acquisition learning and several other DA-dependent behaviors being spared. Moreover, this effect on learning from disappointment was circumscribed to changes in the rate with which mice initiated reward-seeking behaviors, without affecting disengagement dynamics (Tecuapetla et al., 2016). Fitting of the behavior to a reinforcement learning model confirmed that this phenotype is compatible with a selective increase in the learning rate from negative RPEs (Sosa et al., 2021). These findings confirmed our computational predictions of higher pausing efficacy in DA-cNAcc neurons of Ex3d mice and demonstrate that a single alternative splicing mechanism on a subset of neurons can have a conceptually consistent effect on behavior.

Several studies have shown that pause duration and firing rate decreases in DA neurons, as well as reductions in DA release or DA axon Ca^{2+} transients in the ventral striatum, are directly correlated with negative RPE signaling (Bayer et al., 2007; Hart et al., 2014; Menegas et al., 2017; Tian and Uchida, 2015). Furthermore, lesions of the lateral habenula, whose neurons are excited by disappointing and aversive outcomes and disynaptically inhibit DA neurons (Hong et

al., 2011), resulted in blunted firing rate decreases in DA neurons during negative outcomes and affect behavior in a manner that is congruent with a selective reduction in negative RPE signaling (Tian and Uchida, 2015). These pauses are thought to result in a linear reduction of D2R occupancy in striatal projection neurons (Dreyer et al., 2010) and to drive extinction and aversive learning by releasing indirect pathway striatal neuron plasticity from D2R-mediated inhibition (Lee et al., 2021; Shen et al., 2008). Our results add to this literature by showing that negative RPE signaling, based on the inhibition of DA-cNAcc neurons, is under tight biophysical control by a unique K^+ channel modulator. Future studies could therefore use targeted interventions on KChIP4a expression, or Kv4 channel modulation more broadly, to selectively investigate how pauses in DA-cNAcc neurons lead to learning-related processes in target regions.

There are interesting possibilities as to how altered inhibition integration in DA-cNAcc neurons is translated into stronger negative RPE-based learning. A number of effects may be at play in addition to a simple “more consistent inhibition equals enhanced negative RPE signals”. For example, recent studies have shown that, for an unknown reason, shorter optogenetic pauses of DA neurons act as stronger artificial RPEs than longer ones (Chang et al., 2017, 2018). Since the KChIP4a deletion makes pauses more consistent but also restricts their duration, it could be that the effect on pause timing is important for strengthening negative RPE signaling. Another compelling prospect concerns the also recent finding that DA neurons, as a population, encode RPEs in a distributed manner, i.e. individual DA neurons encode RPEs with different biases, so that as a population they are able to fully represent the distribution of probabilistic reward availability statistics (Dabney et al., 2020). Computational modeling further revealed that individual DA neurons fired as if operating with different positive and negative RPE learning rates – α_P and α_N – and therefore were differentially affected by rewarding or disappointing events. The mechanisms that determine this heterogeneity were, however, not determined. We speculate that, by specifically controlling α_N, KChIP4a expression could be important for

controlling this positive/negative RPE signaling bias in each cell. In the case of our study, it could be that removing KChIP4a from DA neurons shifted the population-level encoding of RPEs towards a more “pessimistic” bias, leading to faster extinction.

Our findings may also be relevant for the understanding of human disease. A recent study into the transcriptomes of human midbrain DA neurons found that KCNIP4 expression is a key molecular signature of VTA DA neurons (as opposed to SN DA neurons) and is also strongly associated with DA neuron survival in Parkinson’s disease (Aguila et al., 2021). While this study did not differentiate between different KCNIP4 isoforms, it could be that the differential expression of KChIP4a plays an important role in determining DA neuron vulnerability in Parkinson’s disease, especially since Kv4 current reductions in SN DA neurons have been observed in experimental models of this illness (Subramaniam et al., 2014).

In addition, polymorphisms in the KCNIP4 gene have been linked to multiple mental illnesses, including drug use disorders (Gizer et al., 2017; Han et al., 2013; Johnson et al., 2011; Uhl et al., 2008), attention-deficit-hyperactivity disorder (ADHD) (Lasky-Su et al., 2008; Neale et al., 2008; Weißflog et al., 2013), depression (Perroud et al., 2012; Ripke et al., 2013), bipolar disorder (Sklar et al., 2008; Xu et al., 2014), autism (Hussman et al., 2011), and several personality disorders (Weißflog et al., 2013). Interestingly, most of these polymorphisms are in intronic regions, suggesting that regulatory changes in KCNIP4 gene expression, including alternative splicing, may play a key role in these associations. Furthermore, the diseases most frequently associated with KCNIP4 variations – drug use disorders, ADHD, depression and bipolar disorder – have been linked to altered learning from negative RPEs (Mason et al., 2017; van Meel et al., 2005; Parvaz et al., 2015; Rouhani and Niv, 2019). Our findings suggest the intriguing possibility that KCNIP4 polymorphisms may lead to higher predisposition to specific mental illnesses by changing the regulation of KChIP4a expression and subsequently affecting negative RPE-based learning.

In summary, we have identified KChIP4a as a selective molecular modulator of inhibitory integration in a subset of DA neurons and, consequently, of learning from negative RPEs, singling out this subunit as a likely homeostatic controller of adaptive behaviors. Our findings demonstrate the existence of a highly specialized gene-to-behavior mechanistic chain built within the midbrain DA system. This illuminates how the genetically determined biophysical diversity of DA neurons is critical for the execution of specific computational processes and highlights the importance of uncovering similar mechanisms for understanding how the DA system operates in health and disease.

Acknowledgments

The authors would like to thank Beatrice Fischer, Jasmine Sonntag, and Felicia Müller-Braun for their exceptional technical support. This research was supported by DFG CRC 1080 (A11) to JR and by NIH grant R01DA041705 to CCC and JR. KMC received a one-year fellowship and financial support from the Max Planck Society (International Max Planck Research School for Neural Circuits – MPI for Brain Research).

Author contributions

KMC and JR designed the overarching research project, interpreted all results, and wrote the manuscript. JR supervised the research project. JR and CCC acquired financial support for the research project. KMC wrote the first draft of the manuscript, planned, performed, and analyzed results from behavioral experiments and behavioral modelling, and compiled data from all experiments. NK and JR planned, performed, and analyzed results from the *in vitro* electrophysiology experiments. TM and DS planned, performed, and analyzed results from the combined FISH/IHC assays. JS and BF planned, performed, and analyzed results from the proteomic experiments. CK and CCC developed and implemented the biophysical modelling of DA neurons.

Declaration of Interests

The authors declare no competing interests.

Methods

Resource Availability

Further information and requests for resources and reagents should be directed to and will be fulfilled by the lead contact, Jochen Roeper (roeper@em.uni-frankfurt.de).

Experimental Model and Subject Details

Animal protocols

All animal procedures described in this thesis were approved by the German Regierungspräsidium Gießen and Darmstadt (license numbers: V54-19c 20/15 –FU/1100 & FU1203). Mice were bred and housed until 8 weeks of age at MFD diagnostics (Mainz, Germany). Mice were then maintained under a 12 h dark/light cycle and housed in groups of two to four, with food (R/M-keeping, Ssniff, Germany) and tap water available *ad libitum*, except when they underwent water restriction. Nesting material and a red acrylic glass shelter (mouse house, Tecniplast, Germany) were used as enrichment. For every single experimental procedure in this study, the experimenter was blind to the genotype of the mice and the order in which mice were tested was pseudo-randomized by another team member that was not directly involved in the execution of the experiment.

The DA-neuron selective KChIP4a exon 3 deletion (Ex3d) mouse line

The mouse KChIP4 gene, KCNIP4, is located on chromosome 5 (B3, 48.39 – 49.52 Mb), is 1135 kb in length and has 14 exons, with ATG translation initiation codons in exons 1, 2, 3, 5, and 8, and the STOP codon located in exon 14 (Bethesda (MD): National Library of Medicine (US); National Center for Biotechnology Information, 2017). KChIP4a (a.k.a. KChIP4.4) is a 229

amino acid protein that corresponds to the alternative splicing of exons 3 through 8b of KChIP4, with exon 3 coding for the KID (Deng et al., 2005; Holmqvist et al., 2002).

A new transgenic mouse line was developed for assessing the specific function of the KChIP4a KID using the Cre-lox system. Exon 3 of the KCNIP4 gene (which encodes the KID) was flanked with loxP sites using a vector designed to display two homology regions in a C57BL/6N genetic background, including a short homology region of 1795 bp and a long region of 5858 bp. This vector was electroporated into C57BL/6N embryonic stem cells and screened clones were used for the generation of mice with homozygotic floxing of KCNIP4 exon 3 (*KChIP4-Ex3*$^{lox/lox}$). These mice were then crossed with a line with heterozygous DAT-Cre knock-in (*DAT-Cre*$^{+/-}$ or *DAT-Cre KI*) mice. The offspring of this crossing were then interbred, leading to the production of mice where exon 3 of the KCNIP4 gene was selectively excised from DAT-expressing neurons (Ex3d; *DAT-Cre*$^{+/-}$ / *KChIP4-Ex3*$^{flox/flox}$) and DAT-Cre KI control littermates (CTRL; *DAT-Cre*$^{+/-}$ / *KChIP4-Ex*$^{WT/WT}$).

Genetic identity of all KChIP4-Ex3$^{flox/flox}$ mice was confirmed with polymerase chain reaction (PCR) genotyping throughout the breeding process. For detecting the conditional deletion allele, the following primers were used:

5-TAG TTA TGA CAA GAC AGG AGC TAG TAC CAC TAA GC-3

and

5-GAA CTG GAC TGA AGC AAA ACA AAA CAC G-3.

These primers target the flanking region of the FRT site, and the PCR product lengths were 385 bp for the WT allele and 477 bp for the conditional deletion allele. The PCR protocols were run with 1 cycle at 94 °C for 120s (denaturing), 35 cycles of 94 °C for 30s (denaturing), 65 °C for 30s (annealing) and 68°C for 30s (extension), followed by 1 cycle at 68 °C for 480s (completion).

Method Details

FISH followed by immunofluorescence detection

All steps were conducted at room temperature unless otherwise indicated. 14-µm thick coronal cryosections were post-fixed for 5 min in 4% PFA/PBS, 3 x 5 min washed in PBS (0.1%, diethyl pyrocarbonate [DEPC]) and 1 x 5 min in 1x saline-sodium citrate (SSC, 0.1 % DEPC). Pre-hybridization was performed with 200 µl hybridization buffer (50% formamide, 5x Denhardt's solution, 5x SSC, 0.25 mg/ml yeast tRNA, 0.2 mg/ml salmon sperm DNA, DEPC-H2O) per slide for 4 hrs. Hybridization was performed with 1 ng/µl digoxigenin (DIG)-labelled probes overnight at 65 °C. Probes corresponded to 1) KCHIP4a: NT 1-192 of Mus musculus KCNIP4, transcript variant 4 (NCBI NM_030265.3); 2) KCHIP4 all: NT 455-839 of Mus musculus KCNIP4, transcript variant 4 (NM_001199242.1). Digoxygenin-labeled antisense probes were generated following standard procedures. Post-hybridization washes were performed at 60°C for 5 min in 5x SSC, followed by 5 min in 2x SSC and 20 min in 0.2x SSC/50% formamide. Slides were allowed to cool down for 20 min and washed twice in 0.2x SSC. Endogenous peroxidase activity was quenched by incubation in 3% H2O2/1x SSC for 15 min. Slides were washed twice for 5 min in TBS 1x followed by 30 min blocking in TNB blocking buffer (0.1 M Tris-HCl, 0.15 M NaCl, 0.5 % (w/v) TSA blocking reagent (PerkinElmer)). Slides were incubated in anti-DIG-POD Fab fragments (1:500; Roche) diluted in TNB buffer for 2 hours in a humidified chamber followed by 3 x 10 washing in TBS-T (0.1% Tween-20). Tyramide signal amplification was performed with 100 µl TSA® Plus FITC (1:60; PerkinElmer) per slide for 10 min in a dark chamber. Sections were incubated with Ar6 buffer (1:10; PerkinElmer, Massachusetts) for 45 min in a heat steamer and allowed to cool down for 30 min.

Immunohistochemistry was performed following standard procedures. Briefly, slides were blocked for 30 min in 0.3% Triton / 10% normal goat serum / TBS followed by overnight primary

antibody incubation (1:1000; rb TH; Merck Millipore) at 4 °C. Slides were washed 3 x 10 min in TBS-T and secondary antibody (1:750; Life Technologies) was performed for 1 hr. After 3 x 10 min washing in TBS-T slides were incubated in DAPI 1x for 10 min, washed 3 x 5 min with TBS and embedded in ProLongTM Gold Antifade Mountant (Thermo Fisher Scientific). Images were taken with a Nikon Eclipse90i microscope and acquisition was performed with the NIS Elements software (Version 5.01). Brightness and contrast were moderately enhanced in Photoshop across the entire image, and no further image processing was performed.

Kv4 channel complex high-resolution proteomics

Crude membrane preparation and protein solubilization

Isolated cerebellum and midbrain samples of six CTRL and six Ex3d mice were individually processed. Tissues were homogenized two times in 0.5 ml homogenization buffer (320 mM Sucrose, 10 mM Tris/HCl**,** 1,5 mM MgCl2, 1 mM EGTA, 1 mM Iodoacetamide, pH 7.5) supplemented with protease inhibitors (Aprotinin, Pepstatin, Leupeptin (each at 2 µg/ml) and 1 mM PMSF) with a Dounce homogenizer. Homogenates were centrifuged at 100xg for 5 minutes, resulting supernatants centrifuged at 200.000xg (S45A rotor, Sorvall) for 20 minutes. Pellets were re-suspended in 0.5 ml Lysis-buffer (5 mM Tris/HCl, 1 mM EDTA, 1 mM Iodoacetamide, protease inhibitors) and after 30 minutes incubation time on ice centrifuged at 200.000xg for 20 minutes. The resulting pellets were re-suspended in 0.1 ml 20 mM Tris/HCl pH 7,5 and protein concentrations determined by Bradford assay. 0.3 mg of each sample were solubilized in 0.5 ml CL-48 buffer (Logopharm GmbH, Germany) with freshly added protease inhibitors for 30 minutes on ice. Non-solubilized material was removed by ultracentrifugation (8 min. at 125.000xg, S45A).

Affinity-purifications

Solubilisates were directly incubated with 7,5 µg Kv4.3 antibodies (Alomone, #APC-017) immobilized on Protein A Dynabeads (Invitrogen) for 2 hours at 4°C. Two additional 0.5 ml solubilisates of cerebellum and midbrain samples were incubated with 7,5 µg IgG (Millipore, 12-370), which were used as internal specificity control. After two washing steps with 0.5 ml CL-48 buffer bound proteins were eluted with 1x Laemmli buffer without DTT. Proteins were shortly run on 10% SDS-PAGE and silver-stained. Samples were further processed as described (Schwenk et al., 2012), lanes were split in two pieces and digested with sequencing-grade modified trypsin (Promega, #V5111) and alpha-lytic protease (Sigma-Aldrich, #A6362). Peptides were extracted and prepared for MS analysis.

Mass spectrometry

Mass spectrometric analyses of peptide mixtures were carried out on an Orbitrap Elite hybrid mass spectrometer coupled to an UltiMate 3000 RSLCnano HPLC system (all Thermo Fisher) as described (Schwenk et al., 2019). For each LC-MS/MS dataset, a peak list was extracted from fragment ion spectra using the “msconvert.exe” tool (part of ProteoWizard; http://proteowizard.sourceforge.net/; v3.0.6906; Mascot generic format with filter options “peakPicking true 1-” and “threshold count 500 most-intense”) and the precursor m/z values were shifted by the median m/z offset of all peptides assigned to proteins in a preliminary database search with 50 ppm peptide mass tolerance. Corrected peak lists were searched with Mascot (Matrix Science, UK) against all mouse, rat, and human entries of the UniProtKB/Swiss-Prot database (supplemented with mouse KChIP4 splice isoforms, identifier: Q6PHZ8-2, Q6PHZ8-3, Q6PHZ8-4, Q6PHZ8-5, Q6PHZ8-6). Acetyl (Protein N-term), Carbamidomethyl (C), Gln->pyro-Glu (N-term Q), Glu->pyro-Glu (N-term E), Oxidation (M), and Propionamide (C) were chosen as variable modifications, peptide and fragment mass tolerance were set to ± 5 ppm and ± 0.8 Da, respectively. One missed cleavage was allowed. The expect value cut-off for peptide assignment was set to 0.5.

Protein quantification

Label-free quantification of proteins was done as described previously (Bildl et al., 2012; Muller et al., 2016). Peptide signal intensities (peak volumes, PVs) were determined and offline mass calibrated using MaxQuant (http://www.maxquant.org) and then assigned to peptides based on their m/z and elution time obtained either directly from MS/MS-based identification or indirectly (i.e., from identifications in parallel datasets) using in-house developed software. Molecular abundances of proteins were estimated using the $abundance_{norm,\ spec}$ score defined as the sum of all assigned and protein isoform-specific PVs divided by the number of MS-accessible protein isoform-specific amino acids (Bildl et al., 2012). In order to visualize molecular compositions of Kv4-KChIP complexes normalized molecular abundance values of Kv4.2, Kv4.3 and KCHIP1, 2, 3 and 4, and DDP6 and DPP10, were calculated (Figure 2A and B, and Figure S2). Normalized values were obtained by dividing $abundance_{norm,\ spec}$ values of individual proteins by the factor (∑ of Kv4 abundances/4). Hence, the sum of normalized molecular abundance values for Kv4.2 and Kv4.3 is 4. Relative abundances of KChIP4a isoform in Ex3d versus CTRL samples were determined by use of PV values of 3-5 isoform unique peptide features. For each unique peptide, the PVs were first normalized to their maximum over 12 AP datasets from cerebellum and over 12 AP datasets from midbrain, yielding relative peptide profiles. Accordingly, relative abundance differences of KChIP4a were determined as mean value of peptide profiles from six Ex3d samples and six CTRL samples from cerebellum and midbrain respectively, whereby to the CTRL was set the value of 1 (Figure 2C).

Patch-clamp recordings of projection-identified DA neurons

Retrograde tracing

Mice were premedicated with Carprofen (Rimadyl, Pfizer, Berlin, Germany, 5mg/kg s.c.). Anesthesia was induced and maintained throughout the surgery using isoflurane (AbbVie, North Chicago, USA) Induction: 4% in 350ml/min O2, Maintenance dose: 1-2.5% in 350ml/min O2). For local anesthesia and analgesia, we administered a mixture of Lidocaine and Pirlocaine (EMLA, Aspen, Munich, Germany). After induction of anesthesia, mice were transferred in a stereotaxic frame (Kopf Instruments, Tujunga, CA, USA) where 100nl of red retrobeads (diluted 1:30 in ACSF, Lumafluor, Naples, FL, USA) were injected in different areas of the striatum (in reference to Bregma: NAcc core: AP: 1.54mm, ML: ±1.0mm, DV: 4.0mm; NAcc lateral shell: AP: 0.86mm, ML: ±1.75mm, DV: 4.5mm; DLS: AP: 0.74mm, ML:± 2.2mm, DV: 2.6mm) to label midbrain DA neurons, as previously described (Lammel et al., 2008).

In vitro electrophysiology

After three days of recovery, to ensure sufficient retrograde axonal transport of the red retrobeads, the mice were perfused transcardially using ice cold perfusion solution (125mM NaCl, 2.5mM KCl, 6mM $MgCl_2$, 0.1mM $CaCl_2$, 25mM $NaHCO_3$, 1.25mM NaH_2PO_4, 50mM Sucrose, 2.5mM Glucose, 3mM Kynurenic acid, bubbled with Carbogen). Brains were quickly removed, and the midbrain was sliced into 250µm thick coronal slices using a vibratome (Leica VT1200S, Leica Biosystems, Wetzlar, Germany). Slices were then transferred to a beaker containing ACSF (125mM NaCl, 3.5 mM KCl, 1.2mM $MgCl_2$, 1.2mM $CaCl_2$, 25mM $NaHCO_3$, 1.25mM NaH_2PO_4 constantly bubbled with carbogen) and allowed to recover at 37°C for 60min.

After recovery, slices were transferred to a recording chamber and constantly perfused at a rate of 2-4ml/min^{-1} with ASCF maintained at 37°C (Temperature controller VI, Luigs Neumann, Ratingen, Germany). Synaptic transmission was blocked using CNQX (12.5µM, Biotrend), DL-AP5 (10 µM, Tocris) and Gabazine (4µM, SR95531, Biotrend). Midbrain DA neurons were visualized using a light microscope (Axioskope 2 FS plus, Zeiss, Oberkochen, Germany) and an

infrared camera (VX55, TILL photonics). Red retrobeads were excited by an epifluorescence lamp (HBO100 Nikon) filtered at 546/12nm. DA neurons containing red retrobeads were recorded using borosilicate pipettes (3-4 MOhm, GC150TF, Harvard Apparatus) filled with internal solution (135mM K-gluconate, 5mM KCl, 10mM HEPES, 0.1mM EGTA, 5mM $MgCl_2$, 0.075mM $CaCl_2$, 5mM ATP, 1mM GTP, 0,1% Neurobiotin, pH 7.35 (290-300 mOsmol)). Data were recorded at 20 kHz and filtered with a low-pass filter Bessel characteristic of a 5 kHz cut-off frequency using an EPC 10 amplifier (HEKA Elektronik, Lambrecht, Germany). Patchmaster (HEKA Elektronik, Lambrecht, Germany), IgorPro (WaveMetrics, Portland, Oregon, USA) and MATLAB (MathWorks, Massachusetts, USA) were used for acquisition and analysis. Only spontaneously active cells that showed robust pacemaking, and that were post-hoc identified as TH positive and containing red retrobeads, were included in this study.

Histology

The forebrain tissue-block containing striatal injection sites, as well as midbrain slices containing the recorded and neurobiotin-filled neurons, were immersion-fixed at 4°C overnight in a solution of 4% paraformaldehyde and 15% picric acid in phosphate buffer solution (PBS). Striatal injection sites were cut into 100 µm coronal sections using a vibratome (VT1000S, Leica Biosystems, Wetzlar, Germany). Free-floating sections were washed in PBS and incubated with blocking solution (10% horse serum, 0.5% Triton X-100% and 0.2% BSA in PBS) at room temperature for 1 h. Afterwards, sections were incubated in carrier solution (1% horse serum, 0.5% Triton X-100% and 0.2% BSA in PBS) containing the primary antibody (polyclonal rabbit anti-TH, 1:1000, Synaptic Systems Cat# 213 104) overnight at room temperature. On the second day, sections were washed several times in PBS and incubated with carrier solution containing the secondary antibody (goat anti-rabbit 488, 1:750, Thermo Fisher Scientific Cat# A-11011) and in case of the midbrain sections Streptavidin AlexaFluor 408 (1:750, Invitrogen)

overnight at room temperature. On the third day, sections were washed in PBS, mounted, and stored at 4°C.

Biophysical modelling of DA neurons

Model calibration

The model of a DA-cNAcc neuron was adapted from our newly developed atypical DA neuron model (Knowlton et al., 2021), with modifications to the Kv4.3 channel to allow for independent manipulation of fast (KChIP1-3 and other KChIP4 variants), and slow (KChIP4a) subunits. The model was implemented in NEURON (Hines and Carnevale, 1997) and is a single compartment conductance-based model containing the following channels: voltage gated Na^+ with long term inactivation (NaV1.2), delayed rectifier K^+ (Kdr), an A-type K+ with variable levels of binding to two distinct KChIP populations (Kv4.3), a generic partially inactivating low-threshold Ca^{2+} current (CaL), a generic fully inactivating high threshold Ca^{2+} current (CaH), Ca^{2+} activated K+ channel (SK), and passive leak channels (KL, NaL). Intracellular Ca^{2+} is dynamically buffered and free Ca^{2+} is extruded dynamically via a Ca-ATPase pump (Amini et al., 1999). The calcium pool is constricted to a thin (0.5 um) shell to reflect the calcium dynamics of dendritic compartments where calcium oscillations and corresponding SK activation is most relevant (Kuznetsova et al., 2010; Wilson and Callaway, 2000).

Activation and inactivation kinetics for fast and slow A-type K^+ currents were fit to oocyte data of Kv4.3 with homogenous KChIP1 or KChIP4a expression (Holmqvist et al., 2002). Steady state channel activation and inactivation was set uniformly across subunits, with half activations and slopes adapted from difference current data from VTA DA cells (Tarfa et al., 2017). Consistent with this reference study, the recovery from inactivation was adjusted to allow for saturation of both subunits within 100 ms during hyperpolarizing steps. The time constant of KChIP1 is consistent with the inactivation time constant of Kv4 in lateral shell and striatal projecting cells of

the VTA and SNc that presumably lack KChIP4a. We then make the simplifying assumption that each Kv4 channel only binds to one type of KChIP, and the further assumption that KChIP1-3 and other KChIP4 variants can be grouped together as a single 'fast' KChIP with similar kinetics to KChIP1.

In order to model Kv4.3 in the wildtype core-projecting DA neurons, the ratio of KChIP4a to fast KChIP bound Kv4.3 channels was allowed to vary, and the current due to the two subpopulations of channels was then summed to produce an effective Kv4.3 current. To determine the proper ratio, the difference current between control and simulated Kv4 block during a simulated voltage clamp protocol was fit to a p^3q gating scheme. The ratio of KChIP4a to fast KChIP was adjusted to match the effective inactivation time constant of recorded atypical VTA DA neurons (~250 ms), which include the DA-cNAcc cells. Increasing the proportion of KChIP4a slows the effective inactivation time constant, and a conductance ratio of KChIP4a to fast KChIP of 5:4 (as in the representative control in Figure B) produced the desired value of 250 ms. In the control model, 300 μS/cm^2 of the Kv4 conductance was due to KChiP4a and 240 μS/cm^2 was due to fast KChIPs, for a total of 540 μS/cm^2. In addition to the effects on the channel kinetics, the oocyte data showed that the peak current in Kv4.3 channels exclusively bound to KChIP1 was nearly three times that observed in Kv4.3 channels exclusively bound to KChIP4a (Holmqvist et al., 2002). Therefore, we conservatively doubled the conductance was assigned to KV4.3 channels associated with fast KChIPs compared to those associated with KChIP4a. This results in a 5:2 ratio of KChip4a-bound channels to those bound to fast KChIPs. We assigned a conductance of 60 μS/cm^2 for each part KChIP4a and 120 μS/cm^2 for each part fast KChIP. Deletion of KChIP4a in Ex3d mice was modeled by assuming constant total expression of Kv4.3 channels, leading to a 0:7 ratio with all 840 μS/cm^2 of the conductance now due to fast KChIPs.

Simulated *in vitro* and *in vivo* protocols

Rebound responses to hyperpolarizing currents were recorded in response to a 1s hyperpolarization to -80 mV (-15 pA). Resistance to post-inhibitory depolarization was calculated by applying 10 ms pulses of depolarizing current of variable magnitude at variable times following the termination of the hyperpolarizing pulse.

A simulated *in vivo* environment was created by applying simultaneous applying simultaneous Poisson process trains of excitatory (EPSP) and inhibitory postsynaptic potentials (IPSP). The mean of the exponentially distributed interevent intervals was 10 ms. For the NMDAr train the parameters were 5e-5 μS, Erev=0 mV, and $[Mg^{2+}]$=1.2 mM, whereas for the GABAA train the parameters were 1e-3 μS and Erev=-70 mV (Moradi et al., 2013). These values produce a balanced single spike firing regime state with an average tonic firing rate of 5 Hz (Canavier and Landry, 2006; Komendantov et al., 2004; Lobb et al., 2010). Simulated phasic inhibition, consistent with the signaling of negative RPEs, was generated by increasing the frequency of the $GABA_A$ IPSP train during a 50 ms window at regular 2 s intervals, sufficiently long to eliminate post-rebound transients and not induce entrainment. Spike density histograms were calculated using 500 simulated trial cycles (1000 s). This process was repeated for phasic increases in $GABA_A$ IPSP train mean event frequency ranging from 0 Hz to 1000 Hz in 5 Hz intervals. Note that due to the random nature of the synaptic event generation, the number of synaptic events per phasic event is highly variable even with a fixed noise kernel and allows for a non-integer average number of events. The variance was calculated based on the histogram bins during the 1s prior to each pulse and was calculated independently for each run.

Behavior

Open field

Spontaneous locomotor and exploratory activity (track length, wall distance, time in center and number of rearings) were evaluated in an open field arena (a lidless box measuring 52 × 52 cm, under red illumination at 3 lux) using a video tracking system (Viewer II, Biobserve, Germany) as described in a previous study from our group (Schiemann et al., 2012). For a comprehensive phenotyping of mutant mice, the total track length, the time spent and track length within the center area of the arena (defined as a 30x30 cm square zone with all sides equidistant from the walls), as well as the number and duration of rearings (recorded via infra-red beam breaks at a height of 4.5 cm and defined by being at least 200 ms long and two subsequent rearings had to be at least 80 ms apart), were evaluated. After ten minutes, the mice were returned to their home cages for at least two minutes, and then subjected to the novel object recognition test.

Novel object recognition

A novel object exploration and preference task was used to assess the mice's recognition, memory retention and preference for novel stimuli (Antunes and Biala, 2012; Ennaceur and Delacour, 1988). In this task, mice were placed in the same open field arena described in the previous section, after the open field test (which also served as a habituation for the novel object recognition test), but within the arena two identical objects (stainless steel cylinders; 3 cm diameter x 6 cm height) were placed at equal lengths from each other and at 15 cm from the upper left and right corners. The mice were allowed to freely explore the arena and the objects for 10 minutes (trial 1), after which they were removed from the arena. Subsequently, one of the objects was replaced by a different, novel object (plastic coated rectangular prism; 3x3 cm base x 6 cm height), and the mice were again allowed to explore the arena and the objects (trial 2).

Object recognition was analyzed using Biobserve's Object Recognition plug-in, and object interaction events were defined as periods in which a mouse was directly facing the object (snout directed to the object within a 180° angle) at a distance shorter than 3 cm. Both the number and duration of these interaction events were quantified for both trials of the task. Exploration dynamics (number and duration of objected-directed exploration) were analyzed for both trials, as well as the differences between exploration of an already explored ("old") and novel ("new") object in trial 2, were analyzed. For the quantification of novel object discrimination and preference, a discrimination index was calculated by dividing the difference between the time spent exploring the novel object and the time spent exploring the familiar object by the sum of these two measures (Antunes and Biala, 2012; Ennaceur and Delacour, 1988).

$$DI = \frac{T_{New} - T_{Old}}{T_{New} + T_{Old}}$$

where

DI = discrimination index

T_{New} = time spent exploring the novel object

T_{Old} = time spent exploring the familiar object

<u>Hole board</u>

Exploration of holes, a naturalistic behavior for mice, was evaluated with the hole board task (Crawley, 2007). In this task, mice were placed for five minutes in an open field arena similar to the one used for the open field test, but with 4 circular holes (2 cm in diameter) on its floor (Actimot2, TSE systems). When confronted with such an arena, mice tend to spontaneously

check the holes by dipping their heads in them. The performance of head dips was recorded with infra-red beam breaks placed immediately under the inferior surface of the floor board. The latency to the first head dip, as well as the total number and duration of head dips, were quantified. The percentage of repeated head dips (two dips performed sequentially into the same hole) as well as the percentage of dips into the preferred hole (the hole that was most explored during the session) were also quantified and compared between genotypes.

Spontaneous alternation in the plus maze

Working memory performance was quantified between genotypes using the spontaneous alternation in the plus maze (Ragozzino et al., 1996). Mice were placed in a plastic plus maze (four equidistant 35 x 4.5 cm arms radiating at 90° angles from a circular central arena with 10 cm diameter; walls were 15 cm in height) and allowed free exploration for 12 minutes (Lennartz, 2008). An arm entry was defined as when the mouse enters an arm with all its four paws. Each session was recorded with a video camera and quantification of arm entries was made through visual analysis of the videos. A spontaneous alternation was marked when the mouse explored four different arms in five consecutive arm entries, and the proportion of spontaneous alternations was quantified as the number of real alternations divided by the total possible number of alternations (sum of all arm entries minus four); chance performance in this task is calculated to be 44% (Lennartz, 2008; Ragozzino et al., 1996).

Reinforcement learning task

Male and female Ex3d (N = 10) and CTRL (N = 20) mice, over 8 weeks old, were genotyped and individually identified by the implantation of a subcutaneous transponder microchip (1.4 mm x 9 mm ISO FDX-B glass transponder, Planet ID, Germany). Behavioral comparisons were

performed between Ex3d and DAT-Cre KI mice. One Ex3d mouse showed erratic behavior within the conditioning box and was excluded from data analysis (final N of Ex3d group = 9).

Mice were motivated by water restriction (~85% of their initial body weight) and were rewarded with a solution of 10% sucrose in tap water. Daily water rations varied between 1 and 1.5 mL depending on the mice's weight on that day, with a set target of 85% of the initial body weight. Except during experimental sessions, water was always delivered in a cup placed in their home cage. Mice were also closely monitored in order to ensure that the water supply was consumed and not spilt over or contaminated and the health of the water restricted mice was also evaluated daily (Guo et al., 2014). This protocol was very successful in maintaining stable body weights around the desired target during all experimental sessions (Figure S4) and never resulted in signs of overt dehydration or ill health (e.g. hunched posture or ruffled fur).

The full experimental paradigm spanned 24 days. On the first four days, mice were submitted only to water restriction. In the following two days, they were tamed, i.e. gently handled (held up above their home cage on a spread palm, with no constriction or entrapment by the experimenter) until they no longer tried to escape from the experimenter's hand, showed no overt signs of stress and anxiety and readily drank a portion of liquid reward (0.2 ml) given by the experimenter via a syringe while being held. The following day, the mice were placed inside the operant chamber with the reward port removed for 50 minutes in order to acclimate to the experimental conditions. After this time, they were returned to their home cage and given their daily ration of water. The day after that, mice underwent shaping, i.e. they were placed in the operant chamber for another 50 minutes, now with the reward port present, and at semi-random time intervals (mean of 60 seconds, varying between 30 and 90 seconds), a reward portion (16.66 µL) was delivered at the port, with no cue to its delivery. The following day, mice were submitted to the conditioning task.

The task used in this study is based on the study by Steinberg et al. (Steinberg et al., 2013). In this paradigm, mice learned to associate a CS (sound tone pulsed at 3Hz – 0.1s on/0.2 s off – at 70 dB) to the availability of reward in the reward port. Each session consisted of ten trials (mean ITI of 4 minutes, varying between 1.5 minutes and 6.5 minutes) in which the auditory cue was on for 30 seconds. Mice could trigger reward delivery to the port by entering it during CS presentation. Rewards were delivered in a cycle of 2 s reward delivery (16.66 µL) followed by a 3 s consumption interval. Delivery was continuous for as long as the mouse kept its head in the port during CS presentation. This allowed for a maximum of 6 rewards per trial and a maximum of 60 rewards per session (a total of ~1 mL or reward in the task per day). Additional water supplementation, when needed to complete the mice's daily water ration, was provided in the home cage as described in the previous paragraph.

This acquisition phase lasted for 11 daily sessions. After acquisition, extinction of the conditioned response was tested by consistently omitting the reward during CS presentation for six daily sessions. After extinction, mice were returned to their home cage and received water ad libitum for at least three days before being submitted to other behavioral tasks. All mice recovered their initial body weight in this period of time and showed no long-term adverse effects from water restriction.

Performance in this task was quantified by the total time the mice spent in the port during the cued trials and the latency to enter the port after cue onset. Time in port was normalized both as a percentage of total reward availability time and also by subtracting the amount of time the mouse spend in the port 30 s before cue onset (Steinberg et al., 2013). This means that CS-US associations were quantified by the mouse responding both quickly and selectively to the cue. In addition, the time stamps of every head entry and head retraction into the port were recorded, which allowed the quantification of the dynamics of head entries during cue presentation and during the ITI. Latency was quantified as the time between cue initiation and the first head entry

into the reward port; if mice did not respond in a trial, the maximal possible latency value (30 s) was ascribed to that trial. The dynamics of head entries during extinction were used to infer how the mouse adapts its behavioral response in the absence of an expected reinforcement, i.e. whether it performed fewer head entries (a proxy of the initiation rate of reward-seeking behaviors), head entries that are just shorter in length (indicating a faster disengagement from reward-seeking behaviors) or a combination of both.

Behavioral modelling

A modified Rescorla-Wagner model, which applied two different learning rates for positive (α_P) and negative (α_N) RPEs, was used in order to formally quantify differences in learning between Ex3d and CTRL genotype groups (Raczka et al., 2011; Rescorla and Wagner, 1972; Tian and Uchida, 2015). In detail:

$$if\ (R - V_n)\ \geq 0\ [positive\ RPE]$$

$$V_{n+1} = V_n + \boldsymbol{\alpha_P}(R - V_n)$$

$$if\ (R - V_n) < 0\ [negative\ RPE]$$

$$V_{n+1} = V_n + \boldsymbol{\alpha_N}(R - V_n)$$

where

V = associative strength between CS and US

α_P and α_N = learning rates from positive and negative RPEs, respectively

R = maximal associative strength of the US (reward value)

n = trial index

As a control, the same model was also applied assuming a single learning rate for both positive and negative RPEs, i.e. a classical Rescorla-Wagner model (Figure S5). All modelling and fitting were done with custom MATLAB® code. The percentage of time in port metric was assumed to be a linear read-out of V. The limits of V in relation to the empirical data were bound by the initial value of V before the task (V_0), the lower and upper limits of associative strength readout (V_{min} and V_{max}, respectively). These parameters were derived empirically from each mouse, with V_0 being set as the average response in the first three trials of acquisition, and V_{min} and V_{max} being set as the average responses in the last two sessions of acquisition and extinction, respectively. Fitting of learning rates was performed with least absolute residuals method by implementing the *fminsearch* MATLAB® function (Tian and Uchida, 2015). Goodness of fit was inferred from the residual values of the optimal fit for each mouse.

Quantification and Statistical analyses

For all two-group comparisons, data were tested for normality with the Kolmogorov-Smirnov test. If both distributions were Gaussian, differences were analyzed using two-tailed T-tests; otherwise, the two-tailed Mann-Whitney test was used. Comparisons between groups were evaluated with one-way ANOVA followed by Tukey's multiple comparisons test. Comparisons between groups over multiple trials, sessions or conditions were evaluated using two-way repeated measures ANOVA with Sisak's multiple comparisons *post-hoc* tests. Statistical significance was set at $P < 0.05$ for all comparisons.

References

Aguila, J., Cheng, S., Kee, N., Cao, M., Deng, Q., and Hedlund, E. (2018). Spatial transcriptomics identifies novel markers of vulnerable and resistant midbrain dopamine neurons. BioRxiv 334417.

Aguila, J., Cheng, S., Kee, N., Cao, M., Wang, M., Deng, Q., and Hedlund, E. (2021). Spatial RNA sequencing identifies robust markers of vulnerable and resistant human midbrain dopamine neurons and their expression in Parkinson's Disease. BioRxiv 334417.

Amini, B., Clark, J.W., and Canavier, C.C. (1999). Calcium dynamics underlying pacemaker-like and burst firing oscillations in midbrain dopaminergic neurons: a computational study. J. Neurophysiol. *82*, 2249–2261.

An, W.F., Bowlby, M.R., Betty, M., Cao, J., Ling, H.-P.P., Mendoza, G., Hinson, J.W., Mattsson, K.I., Strassle, B.W., Trimmer, J.S., et al. (2000). Modulation of A-type potassium channels by a family of calcium sensors. Nature *403*, 553–556.

Antunes, M., and Biala, G. (2012). The novel object recognition memory: Neurobiology, test procedure, and its modifications. Cogn. Process. *13*, 93–110.

Bayer, H.M., Glimcher, P.W., Schultz, W., Kimura, M., Sahakian, B.J., and Carter, C.S. (2005). Midbrain dopamine neurons encode a quantitative reward prediction error signal. Neuron *47*, 129–141.

Bayer, H.M., Lau, B., and Glimcher, P.W. (2007). Statistics of midbrain dopamine neuron spike trains in the awake primate. J. Neurophysiol. *98*, 1428–1439.

Berridge, K.C. (2012). From prediction error to incentive salience: mesolimbic computation of reward motivation. Eur. J. Neurosci. *35*, 1124–1143.

Bethesda (MD): National Library of Medicine (US); National Center for Biotechnology Information (2017). National Center for Biotechnology Information (NCBI)[Internet].

Bildl, W., Haupt, A., Müller, C.S., Biniossek, M.L., Thumfart, J.O., Hüber, B., Fakler, B., and Schulte, U. (2012). Extending the dynamic range of label-free mass spectrometric quantification

of affinity purifications. Mol. Cell. Proteomics *11*.

Bromberg-Martin, E.S., Matsumoto, M., and Hikosaka, O. (2010). Dopamine in motivational control: rewarding, aversive, and alerting. Neuron *68*, 815–834.

Canavier, C.C., and Landry, R.S. (2006). An increase in AMPA and a decrease in SK conductance increase burst firing by different mechanisms in a model of a dopamine neuron in vivo. J. Neurophysiol. *96*, 2549–2563.

Chang, C.Y., Esber, G.R., Marrero-Garcia, Y., Yau, H.-J., Bonci, A., and Schoenbaum, G. (2015). Brief optogenetic inhibition of dopamine neurons mimics endogenous negative reward prediction errors. Nat. Neurosci. *19*, 1–8.

Chang, C.Y., Gardner, M., Di Tillio, M.G., and Schoenbaum, G. (2017). Optogenetic Blockade of Dopamine Transients Prevents Learning Induced by Changes in Reward Features. Curr. Biol. *27*, 3480-3486.e3.

Chang, C.Y., Gardner, M.P.H., Conroy, J.C., Whitaker, L.R., and Schoenbaum, G. (2018). Brief, but not prolonged, pauses in the firing of midbrain dopamine neurons are sufficient to produce a conditioned inhibitor. J. Neurosci. *38*, 8822–8830.

Cohen, J.Y., Haesler, S., Vong, L., Lowell, B.B., and Uchida, N. (2012). Neuron-type-specific signals for reward and punishment in the ventral tegmental area. Nature *482*, 85–88.

Costa, K.M. (2014). The Effects of Aging on Substantia Nigra Dopamine Neurons. J. Neurosci. *34*, 15133–15134.

Costa, K.M., Schenkel, D., and Roeper, J. (2021). Sex-dependent alterations in behavior, drug responses and dopamine transporter expression in heterozygous DAT-Cre mice. Sci. Reports | *11*, 3334.

Crawley, J.N. (2007). What’s Wrong With My Mouse? Behavioural Phenotyping of Transgenic and Knockout Mice (Wiley-Interscience).

Dabney, W., Kurth-Nelson, Z., Uchida, N., Starkweather, C.K., Hassabis, D., Munos, R., and Botvinick, M. (2020). A distributional code for value in dopamine-based reinforcement learning.

Nature *577*, 671–675.

Deng, X.-Y., Cai, F., Xia, K., Pan, Q., Long, Z.-G., Wu, L.-Q., Liang, D.-S., Dai, H.-P., Zhang, Z.-H., and XIA, J.-H. (2005). Identification of the Alternative Promoters of the KChIP4 Subfamily. Acta Biochim. Biophys. Sin. (Shanghai). *37*, 241–247.

Dreyer, J.K., Herrik, K.F., Berg, R.W., and Hounsgaard, J.D. (2010). Influence of phasic and tonic dopamine release on receptor activation. J. Neurosci. *30*, 14273–14283.

Ennaceur, A., and Delacour, J. (1988). A new one-trial test for neurobiological studies of memory in rats. 1: Behavioral data. Behav. Brain Res. *31*, 47–59.

Farassat, N., Costa, K.M., Stojanovic, S., Albert, S., Kovacheva, L., Shin, J., Egger, R., Somayaji, M., Duvarci, S., Schneider, G., et al. (2019). In vivo functional diversity of midbrain dopamine neurons within identified axonal projections. Elife *8*.

Gizer, I.R., Bizon, C., Gilder, D.A., Ehlers, C.L., and Wilhelmsen, K.C. (2017). Whole genome sequence study of cannabis dependence in two independent cohorts. Addict. Biol.

Guo, Z.V.Z., Hires, S.A.S., Li, N., O'Connor, D.H.D., Komiyama, T., Ophir, E., Huber, D., Bonardi, C., Morandell, K., Gutnisky, D.D., et al. (2014). Procedures for Behavioral Experiments in Head-Fixed Mice. PLoS One *9*, e88678.

Han, S., Yang, B.-Z., Kranzler, H.R., Liu, X., Zhao, H., Farrer, L.A., Boerwinkle, E., Potash, J.B., and Gelernter, J. (2013). Integrating GWASs and Human Protein Interaction Networks Identifies a Gene Subnetwork Underlying Alcohol Dependence. Am. J. Hum. Genet. *93*, 1027–1034.

Hart, A.S., Rutledge, R.B., Glimcher, P.W., and Phillips, P.E.M. (2014). Phasic dopamine release in the rat nucleus accumbens symmetrically encodes a reward prediction error term. J. Neurosci. *34*, 698–704.

Hines, M.L., and Carnevale, N.T. (1997). The NEURON Simulation Environment. Neural Comput. *9*, 1179–1209.

Holmqvist, M.H., Cao, J., Hernandez-Pineda, R., Jacobson, M.D., Carroll, K.I., Sung, M.A., Betty, M., Ge, P., Gilbride, K.J., Brown, M.E., et al. (2002). Elimination of fast inactivation in Kv4

A-type potassium channels by an auxiliary subunit domain. Proc. Natl. Acad. Sci. U. S. A. *99*, 1035–1040.

Hong, S., Jhou, T.C., Smith, M., Saleem, K.S., and Hikosaka, O. (2011). Negative reward signals from the lateral habenula to dopamine neurons are mediated by rostromedial tegmental nucleus in primates. J Neurosci *31*, 11457–11471.

Hussman, J.P., Chung, R.-H., Griswold, A.J., Jaworski, J.M., Salyakina, D., Ma, D., Konidari, I., Whitehead, P.L., Vance, J.M., Martin, E.R., et al. (2011). A noise-reduction GWAS analysis implicates altered regulation of neurite outgrowth and guidance in autism. Mol. Autism *2*, 1.

Jerng, H.H., and Pfaffinger, P.J. (2008). Multiple Kv channel-interacting proteins contain an N-terminal transmembrane domain that regulates Kv4 channel trafficking and gating. J. Biol. Chem. *283*, 36046–36059.

Jerng, H.H., and Pfaffinger, P.J. (2014). Modulatory mechanisms and multiple functions of somatodendritic A-type K + channel auxiliary subunits. Front. Cell. Neurosci. *8*, 1–20.

Jerng, H.H., Pfaffinger, P.J., and Covarrubias, M. (2004). Molecular physiology and modulation of somatodendritic A-type potassium channels. Mol. Cell. Neurosci. *27*, 343–369.

Johnson, C., Drgon, T., Walther, D., and Uhl, G.R. (2011). Genomic regions identified by overlapping clusters of nominally-positive SNPs from Genome-Wide studies of alcohol and illegal substance dependence. PLoS One *6*.

Kitazawa, M., Kubo, Y., and Nakajo, K. (2014). The stoichiometry and biophysical properties of the Kv4 potassium channel complex with K+ channel-interacting protein (KChIP) subunits are variable, depending on the relative expression level. J. Biol. Chem. *289*, 17597–17609.

Knowlton, C., Costa, K.M., Roeper, J., and Canavier, C.C. (2021). Potentiation of Fast Kv4.3 Subunits in DA-KChIP4a Knockout Mice Strengthens Negative RPE Signaling In Silico. In Virtual Dopamine (ViDA) Conference Abstract, p.

Komendantov, A.O., Komendantova, O.G., Johnson, S.W., and Canavier, C.C. (2004). A Modeling Study Suggests Complementary Roles for GABAA and NMDA Receptors and the SK

Channel in Regulating the Firing Pattern in Midbrain Dopamine Neurons. Https://Doi.Org/10.1152/Jn.00062.2003 *91*, 346–357.

Kramer, D.J., Risso, D., Kosillo, P., Ngai, J., and Bateup, H.S. (2018). Combinatorial expression of Grp and Neurod6 defines dopamine neuron populations with distinct projection patterns and disease vulnerability. ENeuro *5*, 152–170.

Kuznetsova, A.Y., Huertas, M.A., Kuznetsov, A.S., Paladini, C.A., and Canavier, C.C. (2010). Regulation of firing frequency in a computational model of a midbrain dopaminergic neuron. J. Comput. Neurosci. *28*, 389–403.

Lammel, S., Hetzel, A., Häckel, O., Jones, I., Liss, B., and Roeper, J. (2008). Unique Properties of Mesoprefrontal Neurons within a Dual Mesocorticolimbic Dopamine System. Neuron *57*, 760–773.

Lander, E.S., Linton, L.M., Birren, B., Nusbaum, C., Zody, M.C., Baldwin, J., Devon, K., Dewar, K., Doyle, M., FitzHugh, W., et al. (2001). Initial sequencing and analysis of the human genome. Nature *409*, 860–921.

Lasky-Su, J., Neale, B.M., Franke, B., Anney, R.J.L., Zhou, K., Maller, J.B., Vasquez, A.A., Chen, W., Asherson, P., Buitelaar, J., et al. (2008). Genome-wide association scan of quantitative traits for attention deficit hyperactivity disorder identifies novel associations and confirms candidate gene associations. Am. J. Med. Genet. Part B Neuropsychiatr. Genet. *147*, 1345–1354.

Lee, S.J., Lodder, B., Chen, Y., Patriarchi, T., Tian, L., and Sabatini, B.L. (2021). Cell-type-specific asynchronous modulation of PKA by dopamine in learning. Nature *590*, 451–456.

Lennartz, R.C. (2008). The role of extramaze cues in spontaneous alternation in a plus-maze. Learn. Behav. a Psychon. Soc. Publ. *36*, 138–144.

Liss, B., Franz, O., Sewing, S., Bruns, R., Neuhoff, H., and Roeper, J. (2001). Tuning pacemaker frequency of individual dopaminergic neurons by Kv4.3L and KChip3.1 transcription. EMBO J. *20*, 5715–5724.

Lobb, C.J., Wilson, C.J., and Paladini, C.A. (2010). A dynamic role for GABA receptors on the firing pattern of midbrain dopaminergic neurons. J. Neurophysiol. *104*, 403–413.

Mason, L., Eldar, E., and Rutledge, R.B. (2017). Mood instability and reward dysregulation-a neurocomputational model of bipolar disorder. JAMA Psychiatry *74*, 1275–1276.

Matsumoto, H., Tian, J., Uchida, N., and Watabe-Uchida, M. (2016). Midbrain dopamine neurons signal aversion in a reward-context-dependent manner. Elife *5*.

van Meel, C.S., Oosterlaan, J., Heslenfeld, D.J., and Sergeant, J.A. (2005). Telling good from bad news: ADHD differentially affects processing of positive and negative feedback during guessing. Neuropsychologia *43*, 1946–1954.

Menegas, W., Babayan, B.M., Uchida, N., Watabe-Uchida, M., Finke, S., Conzelmann, K., Young, J., Callaway, E., Deisseroth, K., Greene, R., et al. (2017). Opposite initialization to novel cues in dopamine signaling in ventral and posterior striatum in mice. Elife *6*, 751–767.

Moradi, K., Moradi, K., Ganjkhani, M., Hajihasani, M., Gharibzadeh, S., and Kaka, G. (2013). A fast model of voltage-dependent NMDA receptors. J. Comput. Neurosci. *34*, 521–531.

Muller, C.S., Bildl, W., Haupt, A., Ellenrieder, L., Becker, T., Hunte, C., Fakler, B., and Schulte, U. (2016). Cryo-slicing blue native-mass spectrometry (csBN-MS), a Novel technology for high resolution complexome profiling. Mol. Cell. Proteomics *15*, 669–681.

Neale, B.M., Lasky-Su, J., Anney, R., Franke, B., Zhou, K., Maller, J.B., Vasquez, A.A., Asherson, P., Chen, W., Banaschewski, T., et al. (2008). Genome-wide association scan of attention deficit hyperactivity disorder. Am. J. Med. Genet. Part B Neuropsychiatr. Genet. *147*, 1337–1344.

Niv, Y., Duff, M.O., and Dayan, P. (2005). Dopamine, uncertainty and TD learning. Behav. Brain Funct. *1*, 6.

Otomo, K., Perkins, J., Kulkarni, A., Stojanovic, S., Roeper, J., and Paladini, C.A. (2020). In vivo patch-clamp recordings reveal distinct subthreshold signatures and threshold dynamics of midbrain dopamine neurons. Nat. Commun. 2020 111 *11*, 1–15.

Parvaz, M.A., Konova, A.B., Proudfit, G.H., Dunning, J.P., Malaker, P., Moeller, S.J., Maloney, T., Alia-Klein, N., and Goldstein, R.Z. (2015). Impaired Neural Response to Negative Prediction Errors in Cocaine Addiction. J. Neurosci. *35*, 1872–1879.

Perroud, N., Uher, R., Ng, M.Y.M., Guipponi, M., Hauser, J., Henigsberg, N., Maier, W., Mors, O., Gennarelli, M., Rietschel, M., et al. (2012). Genome-wide association study of increasing suicidal ideation during antidepressant treatment in the GENDEP project. Pharmacogenomics J *12*, 68–77.

Raczka, K.A., Mechias, M.-L., Gartmann, N., Reif, A., Deckert, J., Pessiglione, M., and Kalisch, R. (2011). Empirical support for an involvement of the mesostriatal dopamine system in human fear extinction. Transl. Psychiatry *1*, e12.

Ragozzino, M.E., Unick, K.E., and Gold, P.E. (1996). Hippocampal acetylcholine release during memory testing in rats: augmentation by glucose. Proc. Natl. Acad. Sci. U. S. A. *93*, 4693–4698.

Rescorla, and Wagner, A. (1972). A theory of Pavlovian conditioning: Variations in the effectiveness of reinforcement and nonreinforcement.

Ripke, S., Wray, N.R., Lewis, C.M., Hamilton, S.P., Weissman, M.M., Breen, G., Byrne, E.M., Blackwood, D.H.R., Boomsma, D.I., Cichon, S., et al. (2013). A mega-analysis of genome-wide association studies for major depressive disorder. Mol. Psychiatry *18*, 497–511.

Roeper, J. (2013). Dissecting the diversity of midbrain dopamine neurons. Trends Neurosci. *36*, 336–342.

Rouhani, N., and Niv, Y. (2019). Depressive symptoms bias the prediction-error enhancement of memory towards negative events in reinforcement learning. Psychopharmacology (Berl). *236*, 2425–2435.

Schiemann, J., Schlaudraff, F., Klose, V., Bingmer, M., Seino, S., Magill, P.J., Zaghloul, K.A., Schneider, G., Liss, B., and Roeper, J. (2012). K-ATP channels in dopamine substantia nigra neurons control bursting and novelty-induced exploration. Nat. Neurosci. *15*, 1272–1280.

Schultz, W., Dayan, P., and Montague, P.R. (1997). A Neural Substrate of Prediction and

Reward. Science (80-.). *275*, 1593–1599.

Schwenk, J., Harmel, N., Brechet, A., Zolles, G., Berkefeld, H., Müller, C.S., Bildl, W., Baehrens, D., Hüber, B., Kulik, A., et al. (2012). High-Resolution Proteomics Unravel Architecture and Molecular Diversity of Native AMPA Receptor Complexes. Neuron *74*, 621–633.

Schwenk, J., Boudkkazi, S., Kocylowski, M.K., Brechet, A., Zolles, G., Bus, T., Costa, K., Kollewe, A., Jordan, J., Bank, J., et al. (2019). An ER Assembly Line of AMPA-Receptors Controls Excitatory Neurotransmission and Its Plasticity. Neuron *104*, 680-692.e9.

Shen, W., Flajolet, M., Greengard, P., and Surmeier, D.J. (2008). Dichotomous Dopaminergic Control of Striatal Synaptic Plasticity. Science (80-.). *321*, 848–851.

Sklar, P., Smoller, J.W., Fan, J., Ferreira, M.A.R., Perlis, R.H., Chambert, K., Nimgaonkar, V.L., McQueen, M.B., Faraone, S. V, Kirby, A., et al. (2008). Whole-genome association study of bipolar disorder. Mol. Psychiatry *13*, 558–569.

Sosa, R., Mata-Luévanos, J., and Buenrostro-Jáuregui, M. (2021). The Role of the Lateral Habenula in Inhibitory Learning from Reward Omission Experiences. Eneuro ENEURO.0016-21.2021.

Steinberg, E.E., Keiflin, R., Boivin, J.R., Witten, I.B., Deisseroth, K., and Janak, P.H. (2013). A causal link between prediction errors, dopamine neurons and learning. Nat Neurosci *16*, 966–973.

Subramaniam, M., Kern, B., Vogel, S., Klose, V., Schneider, G., and Roeper, J. (2014). Selective increase of in vivo firing frequencies in DA SN neurons after proteasome inhibition in the ventral midbrain. Eur. J. Neurosci. *40*, 2898–2909.

Tang, Y.-Q.Q., Liang, P., Zhou, J., Lu, Y., Lei, L., Bian, X., and Wang, K. (2013). Auxiliary KChIP4a suppresses A-type K+ current through Endoplasmic Reticulum (ER) retention and promoting closed-state inactivation of Kv4 channels. J. Biol. Chem. *288*, 14727–14741.

Tarfa, R.A., Evans, R.C., and Khaliq, Z.M. (2017). Enhanced sensitivity to hyperpolarizing inhibition in mesoaccumbal relative to nigrostriatal dopamine neuron subpopulations. J.

Neurosci.

Tecuapetla, F., Jin, X., Lima, S.Q., and Costa, R.M. (2016). Complementary Contributions of Striatal Projection Pathways to Action Initiation and Execution. Cell *166*, 703–715.

Tian, J., and Uchida, N. (2015). Habenula Lesions Reveal that Multiple Mechanisms Underlie Dopamine Prediction Errors. Neuron *87*, 1304–1316.

Uhl, G.G.R., Liu, Q.-R.Q., Drgon, T., Johnson, C., Walther, D., Rose, J.E., David, S.S.P., Niaura, R., and Lerman, C. (2008). Molecular genetics of successful smoking cessation: convergent genome-wide association study results. Arch. Gen. Psychiatry *65*, 683.

Weißflog, L., Scholz, C.J., Jacob, C.P., Nguyen, T.T., Zamzow, K., Groß-Lesch, S., Renner, T.J., Romanos, M., Rujescu, D., Walitza, S., et al. (2013). KCNIP4 as a candidate gene for personality disorders and adult ADHD. Eur. Neuropsychopharmacol. *23*, 436–447.

Wilson, C.J., and Callaway, J.C. (2000). Coupled oscillator model of the dopaminergic neuron of the substantia nigra. J Neurophysiol *83*, 3084–3100.

Xu, W., Cohen-Woods, S., Chen, Q., Noor, A., Knight, J., Hosang, G., Parikh, S. V, De Luca, V., Tozzi, F., Muglia, P., et al. (2014). Genome-wide association study of bipolar disorder in Canadian and UK populations corroborates disease loci including SYNE1 and CSMD1. BMC Med. Genet. *15*, 2.

Zhou, J., Tang, Y., Zheng, Q., Li, M., Yuan, T., Chen, L., Huang, Z., and Wang, K. (2015). Different KChIPs Compete for Heteromultimeric Assembly with Pore-Forming Kv4 Subunits. Biophys. J. *108*, 2658–2669.

Supplemental figures

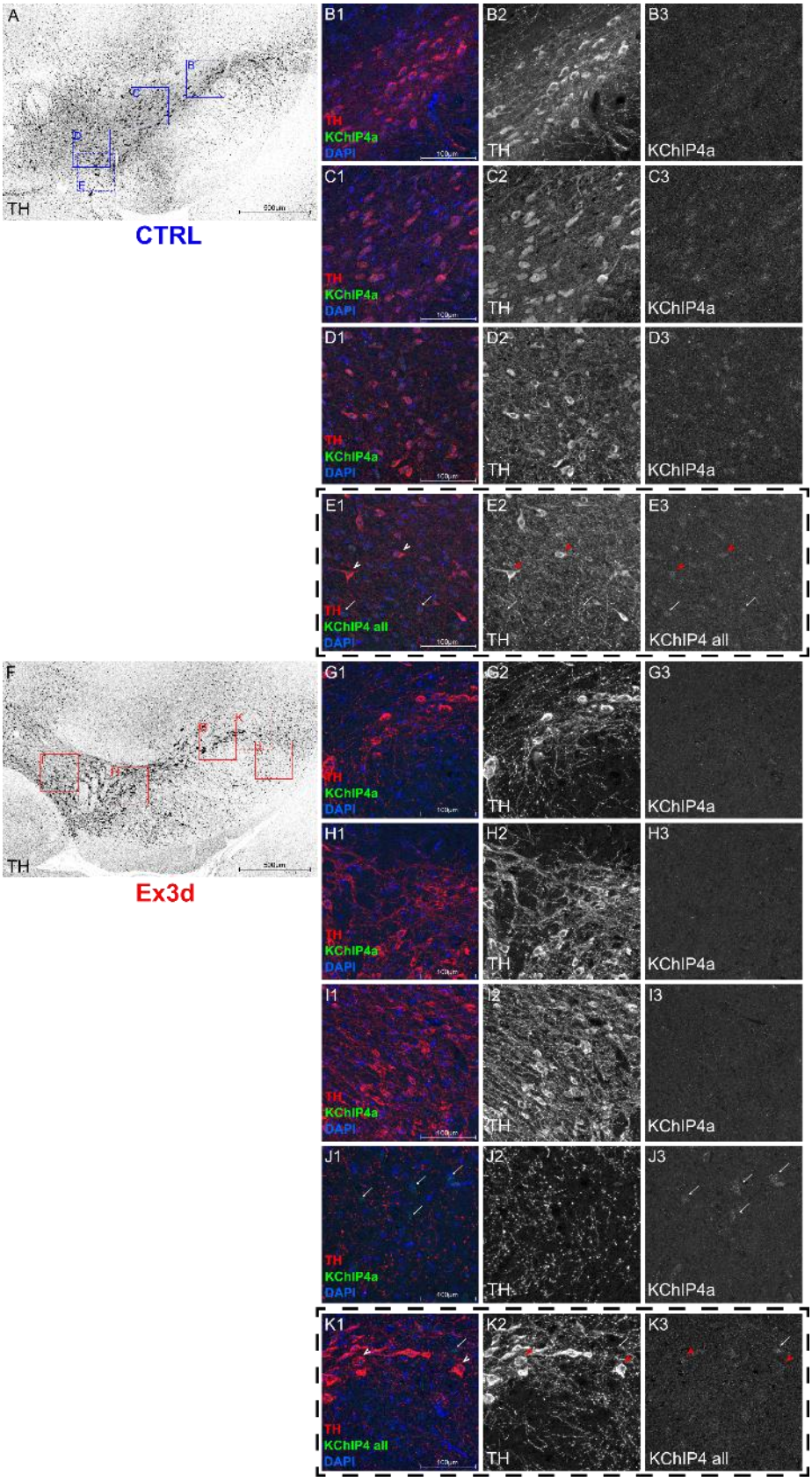

Figure S1. FISH assay confirms that Ex3d mice have a selective ablation of only KChIP4a mRNA expression specifically in DA neurons, related to Figure 1.

A: Overview of a midbrain slice from a CTRL mouse where the indicated rectangles represent the ROIs used for panels B-E. **B-C:** FISH labeling with the KChIP4a-specific probe reveals that CTRL mice show robust expression of KChIP4a mRNA in TH^+ and TH^- neurons across the whole midbrain. **E:** Labeling with the general KChIP4 probe, which binds to all KChIP4 isoforms, also shows expression in midbrain TH^+ and TH^- neurons. **F:** Overview of a midbrain slice from an Ex3d mouse where the indicated rectangles represent the ROIs used for panels G-K. **G-I:** unlike in the CTRLs, labeling with the KChIP4a-specific probe showed that there was no expression of KChIP4a in TH^+ neurons across the whole midbrain of Ex3d mice, including the SN and VTA. **J:** However, we did observe robust KChIP4a expression in midbrain TH^- neurons, demonstrating that the removal of KChIP4a was cell-type specific. K: Labeling with the general KChIP4 probe showed expression of KChIP4 variants in TH+ neurons in the midbrain of Ex3d mice, demonstrating that the removal of KChIP4a was also splice variant-specific.

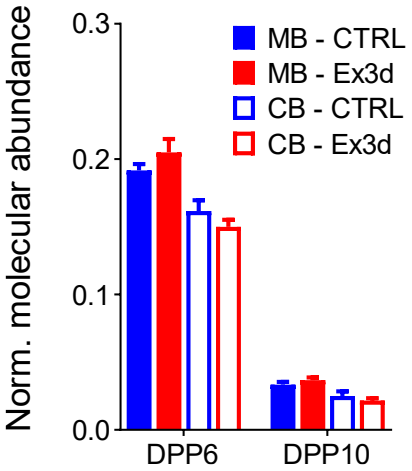

Figure S2. Relative abundance of DPPX proteins bound to Kv4 channels in the midbrain and in the cerebellum, related to Figure 2.

We found relatively low abundance of DPP6 and DPP10 proteins bound to Kv4 channel complexes in both the MB and CB. Importantly, there was no effect of the Ex3d mutation in either region.

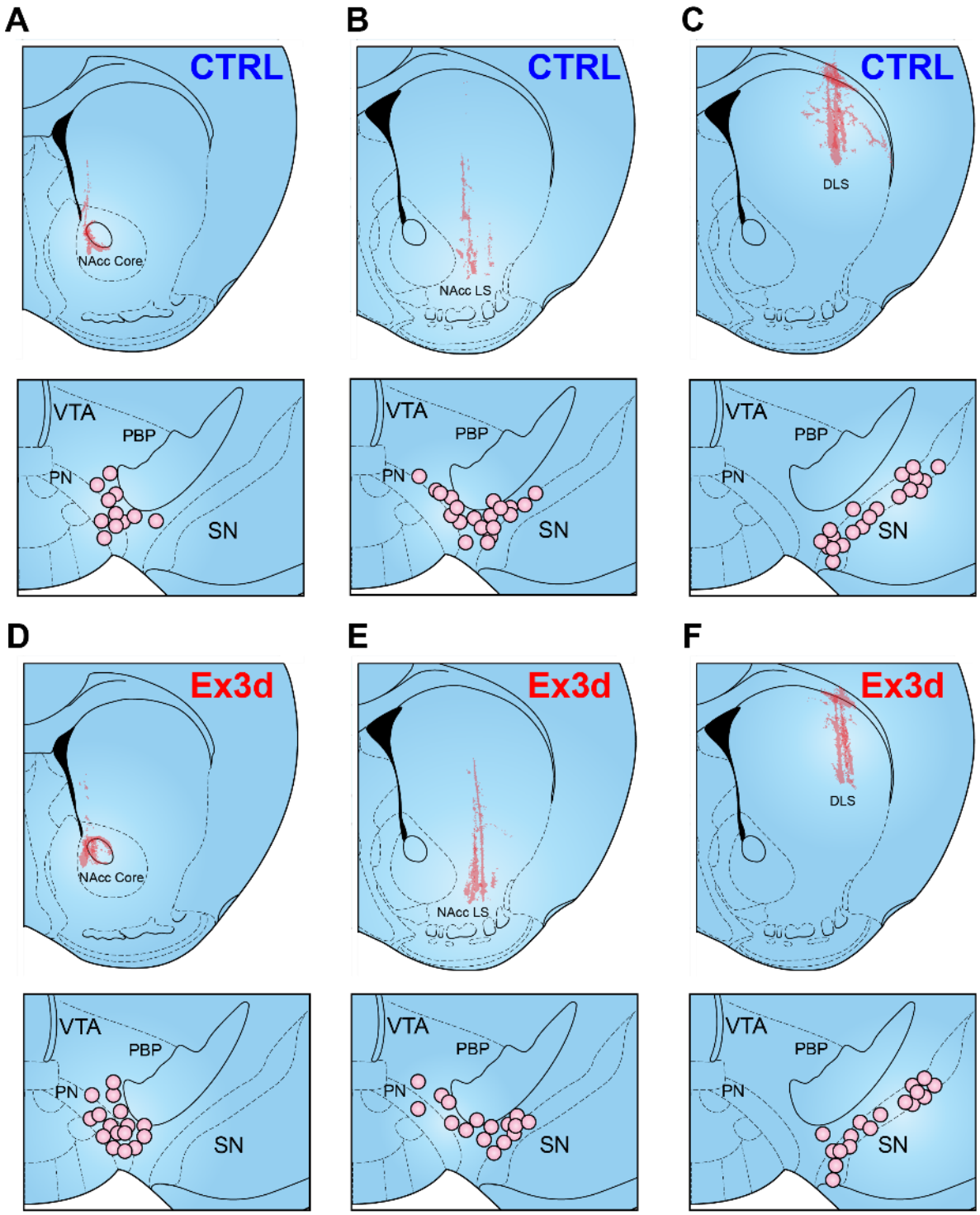

Figure S3. red retrobead injection sites and recording locations for projection-specific patch-clamp experiments, related to Figure 3.

A, B, C: Spread of all red retrobead injections and location of projection-identified TH+ cells in the midbrain for the DA-cNAcc (A), DA-lNAcc (B) and DA-DLS (C) neuronal populations in CTRL mice. **D, E, F:** Same as above, but for Ex3d mice.

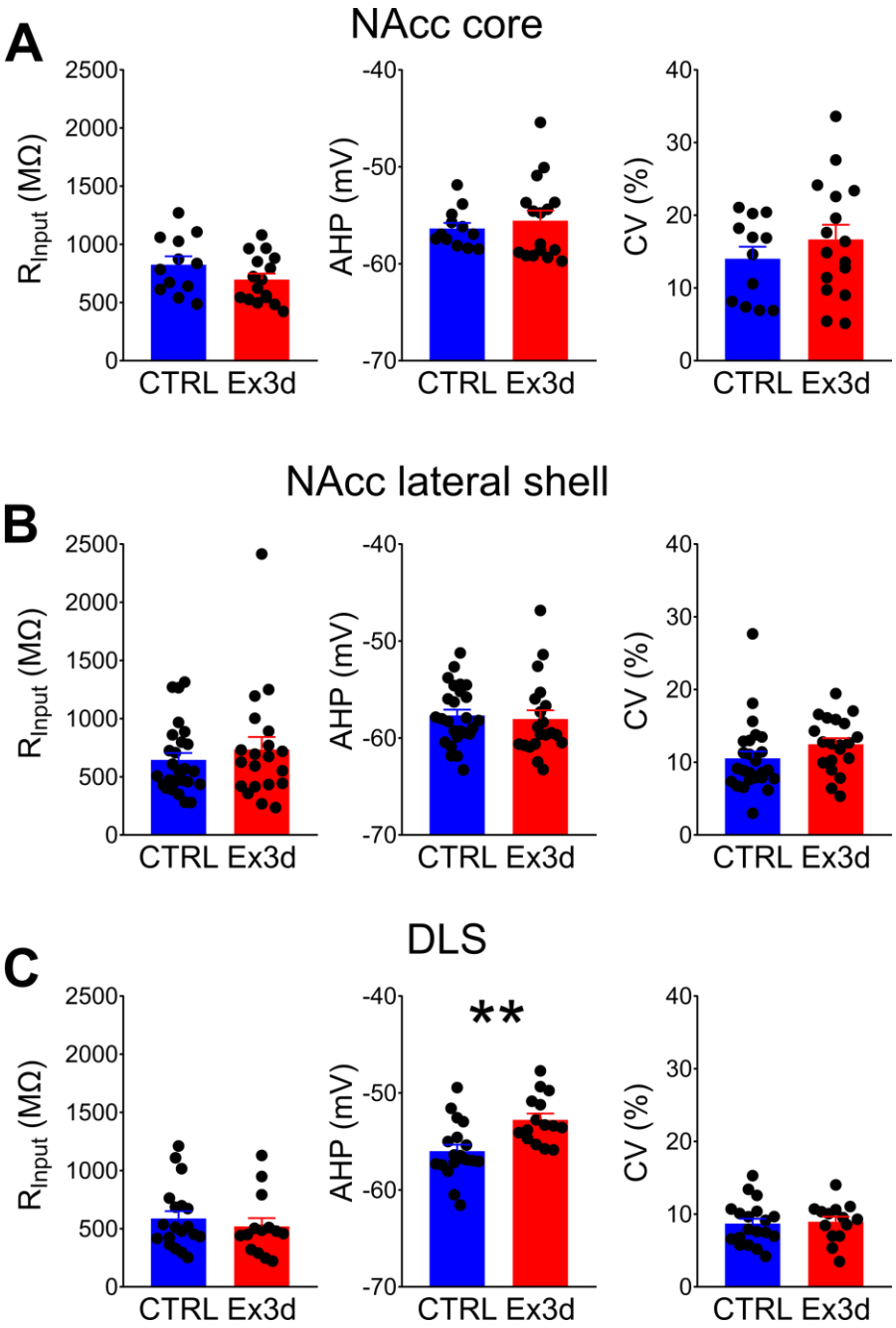

Figure S4. Additional biophysical properties of the recorded DA neuron subpopulations are not affected by the Ex3d mutation, related to Figure 3.

A: Values of input resistance (R_{input}), afterhyperpolarization (AHP) and inter-spike-interval coefficient of variation (CV) for DA-cNAcc projecting neurons of CTRL and Ex3d mice. **B, C:** same as above, but for DA-lNAcc and DA-DLS neurons. Note there were no significant genotype effects for any of these variables in any of the projection-identified populations, with the exception of an increase in the minimum AHP in DA-DLS neurons.

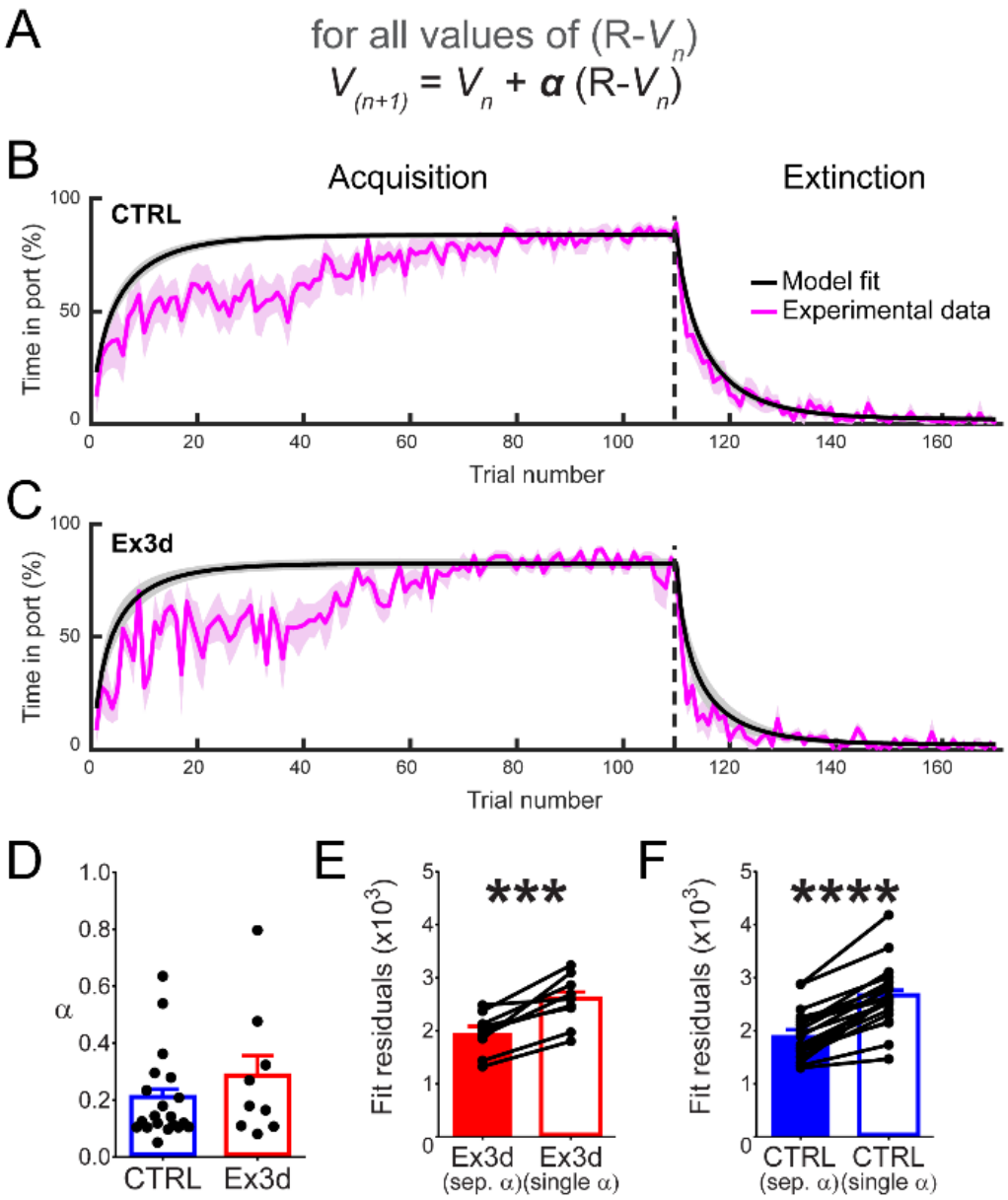

Figure S5. Models that do not assume different learning rates for positive and negative RPEs produce significantly worse fits and do not replicate the observed Ex3d behavioral phenotype, related to Figure 6.

A: Equation of the traditional Rescorla-Wagner model used as a control. **B, C:** Comparison of model fits and experimental data for the CTRL (B) and Ex3d (C) group. **D:** fitted learning rates for CTRL and Ex3d data. Note the lack of genotype differences. E, F: comparison of fit residuals between models with a single learning rate and with separate positive and negative learning rates for the Ex3d (E) and CTRL (F) groups. Note that single learning rate models are significantly worse at fitting the behavioral data.